Titre: Title:	Self-sorting of bidisperse particles in evaporating sessile droplets
Auteurs: Authors:	Aman Jain, Fabian Denner, & Berend van Wachem
Date:	2025
Type:	Article de revue / Article
Référence: Citation:	Jain, A., Denner, F., & van Wachem, B. (2025). Self-sorting of bidisperse particles in evaporating sessile droplets. International Journal of Multiphase Flow, 193, 105382 (20 pages). https://doi.org/10.1016/j.ijmultiphaseflow.2025.105382

URL de PolyPublie: PolyPublie URL:	https://publications.polymtl.ca/67097/
Version:	Version officielle de l'éditeur / Published version Révisé par les pairs / Refereed
Conditions d'utilisation: Terms of Use:	Creative Commons Attribution 4.0 International (CC BY)

Titre de la revue: Journal Title:	International Journal of Multiphase Flow (vol. 193)
Maison d'édition: Publisher:	Elsevier BV
URL officiel: Official URL:	https://doi.org/10.1016/j.ijmultiphaseflow.2025.105382
Mention légale: Legal notice:	© 2025 The Authors. Published by Elsevier Ltd. This is an open access article under the CC BY license (http://creativecommons.org/licenses/by/4.0/)

International Journal of Multiphase Flow 193 (2025) 105382

Contents lists available at ScienceDirect

International Journal of Multiphase Flow

journal homepage: www.elsevier.com/locate/ijmulflow

Research paper

Self-sorting of bidisperse particles in evaporating sessile droplets

Aman Kumar Jain [a], Fabian Denner [b], Berend van Wachem [a],*

[a] Chair of Mechanical Process Engineering, Otto-von-Guericke-Universität Magdeburg, Universitätsplatz 2, 39106 Magdeburg, Germany
[b] Department of Mechanical Engineering, Polytechnique Montréal, Montréal, H3T 1J4, Québec, Canada

ARTICLE INFO

Dataset link: https://doi.org/10.5281/zenodo.15114147

Keywords:
Sessile droplet
Evaporating droplet
Bidisperse particles
Particle self-sorting
VOF-DEM
Marangoni flow

ABSTRACT

This study investigates the dispersion and self-sorting dynamics of bidisperse particles, *i.e.*, a mixture of two distinct particle sizes, during the evaporation of ethanol droplets on a heated substrate, focusing on the influence of surface wettability, Marangoni stresses, and relative particle density. To this end, numerical simulations are carried out using a two-stage numerical approach: the first stage simulates the gas-liquid flow along with the heat and vapor distribution, while the second stage models the particle behavior using Lagrangian particle tracking. The results reveal that for an ethanol droplet evaporating with a constant contact angle in the absence of thermocapillary Marangoni stresses, the flow induced by the receding motion of the contact line supersedes the capillary flow, moving the fluid from the contact line to the apex of the droplet. This flow moves the particles from the bulk of the droplet to the apex of the droplet and suppresses size-based self-sorting of the particles. However, in the presence of Marangoni stresses, a flow along the interface near the apex of the droplet promotes the self-sorting of particles based on their size, whereby smaller particles concentrate near the droplet apex and larger particles form an outer shell around them.

1. Introduction

Sessile droplets are encountered in many industrial and technological applications (Zang et al., 2019), such as inkjet printing (Yoo and Kim, 2015), spray cooling, and medical diagnostics (Chen et al., 2016). Even though sessile droplets frequently occur, describing them accurately is a complex process, as they involve mass and heat transfer, as well as the motion of the three-phase contact line. In addition, Marangoni convection resulting from temperature and solutal gradients as well as the wettability of the substrate affects the motion of the contact line, which in turn affects the flow within the droplet (Snoeijer and Andreotti, 2013). In the literature, two main evaporation modes of sessile droplets are often distinguished (Gelderblom et al., 2022): droplets with a constant contact radius and varying contact angle, often referred to as constant contact radius (CCR) mode, and droplets with a varying contact radius and constant contact angle, often referred to as constant contact angle (CCA) mode. In reality, depending on the receding contact angle for a given solid–liquid combination and on self-pinning due to deposits, a droplet either evaporates in the CCR mode or CCA mode (Larson, 2014). The substrate properties can, as is done in many engineering applications, be tailored to achieve a desired motion of the contact line, thereby steering the flow inside the droplet and, consequently, the particle deposition on the substrate (Iqbal et al., 2022).

To understand the nature of the deposition, it is important to understand the heat, mass, and momentum transport within the droplet during evaporation, the behavior of the three-phase contact line, and the interaction of particles with the interface of the droplet and substrate (Larson, 2014; Erdem et al., 2024). The deposition pattern can be of several forms, with the most common being a “coffee ring” deposit (Deegan, 2000) along with the coffee-eye, concentric rings, cracks, or wrinkling (Mondal et al., 2023). Usually, these non-uniform deposits are regarded as defects in industrial processes and efforts are made to obtain a uniform deposition, which requires an in-depth understanding of the phenomenon related to sessile droplet evaporation and particle dispersion.

In the case of the evaporation of a sessile droplet on a heated substrate, the flow inside the droplet is primarily affected by thermal Marangoni stresses and the contact line motion. In our previous work (Jain et al., 2024), we show that for a pinned ethanol droplet evaporating on a heated substrate, the flow inside the droplet, the temperature distribution, and the particle dispersion are significantly affected by the presence of thermal Marangoni stresses. Generally, when a droplet evaporates, the CCR mode dominates the evaporation process until the receding contact angle is reached (Hu and Larson, 2002). As a result, the CCR evaporation mode has been extensively studied. However, it is possible to “choose” or engineer the solid

---

* Corresponding author.
E-mail address: berend.van.wachem@multiflow.org (B. van Wachem).

https://doi.org/10.1016/j.ijmultiphaseflow.2025.105382
Received 1 April 2025; Received in revised form 20 June 2025; Accepted 27 July 2025

surface properties such that droplets evaporate in CCA mode to obtain a deposit pattern other than a coffee ring (Wang and Wu, 2013). Dash and Garimella (2013) experimentally show that droplets evaporating in CCA mode on a super-hydrophobic substrate require a longer time to evaporate as predicted by a classical diffusion model. The reason for this observation is a reduced evaporation rate caused by evaporative cooling at the droplet interface, leading to a longer thermal resistance path, and the low effective conductivity of the substrate owing to the relatively small solid–liquid contact area. For a droplet evaporating in CCA mode or with a moving contact line, along with the capillary and Marangoni flows, an additional inward flow away from the contact line is introduced because of the receding motion of the contact line (Berteloot et al., 2008). These three types of flow inside an evaporating droplet with moving contact line play a dominant role in the dispersion and deposition of particles inside the droplet.

Nguyen et al. (2013) describe the experimental observation that the evaporation of a water droplet containing silica particles and with a moving contact line on a smooth hydrophobic surface results in an inner coffee ring deposit, containing different dendrite deposit patterns with a radius smaller than the initial contact radius. Similarly, Das et al. (2017) experimentally show that coating a glass substrate with silicone causes water droplets to evaporate in the CCA mode 75% of the time, which suppresses the coffee-ring deposition of silica particles and promotes ordered crystal growth at the center of the droplet. They also suggest that a low evaporation rate of the droplet favors the formation of more ordered structures in the final aggregate. Yang et al. (2020) show that the hydrophobicity of the substrate can be altered by coating silicon wafers with alkysilane to experimentally study the colloidal deposition of silica particles from a water droplet evaporating in the depinned mode. They show that the particle concentration near the contact line required for the pinning of the contact line depends linearly on the receding contact angle of the surface, irrespective of the substrate material and initial particle concentration. Furthermore, they report that the required particle concentration decreases with increasing particle size and that the large particles of bidisperse silica suspensions dominate the self-pinning process. Another experimental study by Gupta et al. (2023) of water droplets with polystyrene particles on a hydrophobic PDMS surface, show that for a monodisperse particle population, the initial pinning stage is higher for smaller particles than for larger particles, and that the depinning of droplets containing bidisperse particles is delayed compared to monodisperse particles. They also investigated the effect of substrate heating and showed that, as the substrate temperature increases, the initial pinning stage is extended due to the combined action of thermal Marangoni and outward-driven radial evaporative flows at elevated temperatures, and the number of particles near the contact line increases, thereby promoting self-pinning.

Often, physical processes involving particle deposition from sessile droplets contain particles that vary in size (Zolotarev and Kolegov, 2022), and the particles may be segregated or classified during the dispersion and deposition inside the droplet. Chhasatia and Sun (2011) experimentally describe the deposition behavior of a mixture of micro- and nano-particles in a water droplet onto a glass substrate with different wettabilities. Their experiments show that the CCA mode dominates the evaporation process on a hydrophobic substrate, such that the particles do not deposit until the later stages of the droplet evaporation, at which point only little carrier liquid is left to facilitate particle classification. However, increasing the surface wettability improves particle sorting, particularly near the contact line when the droplet evaporates in the CCR mode.

Several numerical studies have been conducted with the aim of understanding the behavior of evaporating sessile droplets with a moving contact line (Paul and Dhar, 2023; Shang et al., 2024; Zhu et al., 2021; Bhardwaj, 2018; Erdem et al., 2024). Paul and Dhar (2023) applied the finite-element method to study the transients of the Stefan and Marangoni advection during the evaporation of both pinned and depinned sessile droplets. They report that for droplets evaporating in depinned mode, the temperature and velocity fields at the intermediate stages remained qualitatively similar to those of the initial conditions, and in the later stages, evaporative cooling dominates, due to the lower conductivity from the smaller solid–liquid contact area and enhanced evaporative mass flux from liquid-vapor interface, which is inversely proportional to the droplet contact radius. The prevailing challenges in modeling the flow inside evaporating sessile droplets are highlighted in the studies of Petsi and Burganos (2008) and Bhardwaj (2018). Assuming the flow inside an evaporating sessile droplet is accurately described as a two-dimensional Stokes flow, the results reported in Petsi and Burganos (2008) suggest that for contact angles less than 90° the flow is directed towards the center of the droplet, whereas for contact angles larger than 90° the flow is directed towards the contact line of the droplet. In Bhardwaj (2018), an expression for the evaporation mass rate for a hydrophobic surface using a scaling analysis to estimate the direction and magnitude of the characteristic evaporation-driven flow velocity inside the droplet is proposed, suggesting that for a contact angle less than 90° the flow is directed towards the contact line of the droplet, whereas for contact angles greater than 90° the flow is directed towards the center of the droplet. These studies mainly focus on the evaporation flux and the flow inside the droplet, which eventually affects the dispersion of the particles in the droplet.

In this study, we investigate the behavior of bidisperse particles, *i.e.*, a particle mixture with two distinct particle sizes, in sessile droplets with a moving contact line as they evaporate. To this end, we use a finite-volume method to model the gas-liquid fluid flow, in conjunction with Lagrangian particle tracking to model the particle behavior, based on our previous work (Jain et al., 2024). Considering three different contact angles of the droplet and two different particle sizes, our study focuses primarily on the influence of the thermocapillary Marangoni stresses and the contact angle on the fluid flow inside an ethanol droplet evaporating on a heated substrate, as well as the resulting dispersion and size-based sorting of particles inside the droplet and at the gas-liquid interface.

The remainder of this paper is organized as follows. In Section 2, we discuss the volume of fluid (VOF) and the discrete element model (DEM) frameworks which are used in this study. In Section 3, we detail the configuration of various simulation cases and the different physical parameters governing the problem are given. In Section 4, we validate the employed numerical framework and chosen mesh resolution for the evaporating sessile droplets with a moving contact line by comparing the numerical results to analytical solutions and experimental measurements. Subsequently, we investigate the flow and temperature distribution inside the droplet (Section 5) as well as the particle dispersion and self-sorting (Section 6), considering or neglecting the Marangoni stresses, and varying the relative density of the particles compared to the density of the fluid. Section 7 presents the conclusions of this study.

2. Methodology

In this study, we consider bidisperse particle populations varying in size that are simulated in sessile droplets evaporating with a moving contact line on a heated substrate. To facilitate this, our existing model for pinned sessile droplets with monodisperse particles (Jain et al., 2024) is modified to account for a moving contact line and bidisperse particles.

For an evaporating ethanol droplet with a constant contact angle of $\theta_c \in \{60^\circ, 90^\circ, 120^\circ\}$ and an initial radius of $R_c = 0.5$ mm, the Bond number varies from $\mathrm{Bo} = 0.049 - 0.1475 \ll 1$, suggesting that the droplet maintains a spherical shape throughout the simulation. Similar to our previous work (Jain et al., 2024), it can be shown that the Péclet number for vapor transport in the gaseous phase is less than 1; thus, we can assume that vapor transport in the gas phase is dominated by diffusion. However, the Péclet number for heat transport in the liquid phase due to Marangoni convection is larger than 10, suggesting that heat transport due to convection inside the liquid cannot be neglected. The total volume fraction of the particles inside the droplet is less than 1% and we, thus, assume that the particles have a negligible influence on the fluid flow. This allows us to reduce the computational cost by applying one-way coupling, where the fluid influences the motion of the particles, but the particles do not influence the fluid flow.

2.1. Gas-liquid flow model

To simulate the gas-liquid system of an evaporating sessile droplet and its surrounding fluid, a second-order finite-volume method is employed (Denner and van Wachem, 2014b). This model comprises three key elements: the equations that govern the two-phase flow (Section 2.1.1), the volume of fluid (VOF) method (Denner and van Wachem, 2014b) to capture the behavior of the gas-liquid interface (Section 2.1.2), and a model for the heat and mass transfer (Section 2.1.3).

2.1.1. Fluid flow equations

The gas-liquid flow in and around the droplet is modeled using the one-fluid formulation of the incompressible continuity and momentum equations, given as

$$\nabla \cdot \boldsymbol{u} = -\dot{m}\left(\frac{1}{\rho_\mathrm{l}} - \frac{1}{\rho_\mathrm{v}}\right), \tag{1}$$

$$\rho\left(\frac{\partial \boldsymbol{u}}{\partial t} + \nabla \cdot (\boldsymbol{u} \otimes \boldsymbol{u})\right) = -\nabla p + \nabla \cdot (\mu(\nabla \boldsymbol{u} + \nabla \boldsymbol{u}^T)) + \boldsymbol{f}_\mathrm{s}, \tag{2}$$

where $\boldsymbol{u}$ is the fluid velocity vector, $\dot{m}$ is the fluid mass flux due to evaporation, ρ is the fluid density, p is the pressure, μ is the fluid viscosity, and $\boldsymbol{f}_\mathrm{s}$ is the volumetric force representing the surface tension. Due to the low Bond number of the considered droplet, gravity is neglected when solving the fluid flow. The volumetric force representing surface tension in the presence of temperature variations is given as (Brackbill et al., 1992; Kothe et al., 1996)

$$\boldsymbol{f}_\mathrm{s} = \sigma\kappa\nabla\alpha + \nabla_\mathrm{s}\sigma|\nabla\alpha|, \tag{3}$$

where α is the liquid volume fraction (see Section 2.1.2), κ is the interface curvature, and $\nabla_\mathrm{s}\sigma$ is the gradient of the surface tension coefficient tangential to the interface. The surface tension coefficient σ is assumed to vary linearly with the temperature and is defined as $\sigma = \sigma_0 + \sigma_\mathrm{T}(T - T_0)$, such that

$$\nabla_\mathrm{s}\sigma = \sigma_\mathrm{T}[\nabla T - (\nabla T \cdot \boldsymbol{n})\boldsymbol{n}], \tag{4}$$

where T is the temperature, σ_0 is the surface tension coefficient at the reference temperature T_0, σ_T is the temperature coefficient of the surface tension, and $\boldsymbol{n}$ is the normal vector of the interface.

2.1.2. Gas-liquid interface

The gas-liquid interface is described using the VOF method, where the liquid volume fraction α is defined as

$$\alpha = \begin{cases} 1 & \text{in the liquid phase,} \\ 0 & \text{in the gas phase,} \end{cases} \tag{5}$$

with $0 < \alpha < 1$ signifying the presence of the gas-liquid interface. The value of α is used to define the local fluid properties, such as the density, viscosity, specific heat capacity, thermal diffusivity, and the mass diffusion coefficient. In our work, the volume fraction evolves only as a result of the evaporative mass flux, such that

$$\frac{\partial \alpha}{\partial t} = -\frac{\dot{m}}{\rho_\mathrm{l}}. \tag{6}$$

It should be noted that in this equation the advection term is neglected, since considering the evaporative flux for the interface advection directly eliminates the need for any special treatment of the Stefan flux (Jain et al., 2024). To maintain the spherical shape of the droplet, regular re-initialization is carried out.

2.1.3. Heat and mass transfer

The evaporation model combines solving for the vapor concentration and the thermal energy of the fluid. Based on the compressive continuous species transfer model (C-CST) (Haroun et al., 2010; Marschall et al., 2012; Deising et al., 2016; Zanutto et al., 2022), the temperature T and vapor mass concentration c are calculated using a one-field energy equation,

$$\rho C_\mathrm{p}\left(\frac{\partial T}{\partial t} + \boldsymbol{u} \cdot \nabla T\right) = \nabla \cdot (k\nabla T) - \dot{m}L, \tag{7}$$

$$\frac{\partial c}{\partial t} = \nabla \cdot (D\nabla c + \boldsymbol{\phi}), \tag{8}$$

where k represents the thermal conductivity, C_p the specific heat capacity, L is the latent heat of vaporization, and D represents the effective diffusion coefficient of the vapor. The term $\boldsymbol{\phi}$ represents the flux that results from the concentration jump at the fluid/fluid interface. Neglecting the advection term in Eq. (8) is justified because the Péclet number of the vapor transport is less than 1, suggesting that diffusion is the dominant transport mechanism of the vapor (Jain et al., 2024). The calculation of the effective diffusion coefficients D and $\boldsymbol{\phi}$ has been detailed in our previous work (Zanutto et al., 2022; Jain et al., 2024). The calculation of the mass flux due to evaporation, $\dot{m}$, is approximated by Fick's law, as explained by Zanutto et al. (2022) and Maes and Soulaine (2020), where $\dot{m}$ is defined as

$$\dot{m} = \frac{(D\nabla c - \boldsymbol{\phi})}{1 - \alpha} \cdot \nabla\alpha, \tag{9}$$

2.2. Discrete element method

Newton's second law of motion is applied to describe the particle motion and the discrete element method (DEM) is employed to simulate interactions between particles and the substrate (Cundall and Strack, 1979). The translational and rotational motion of each particle is determined by

$$m_\mathrm{p}\frac{\mathrm{d}\boldsymbol{v}_\mathbf{p}}{\mathrm{d}t} = m_\mathrm{p}\left(1 - \frac{\rho_\mathrm{f}}{\rho_\mathrm{p}}\right)\boldsymbol{g} + \boldsymbol{f}_\mathrm{c} + \boldsymbol{f}_\mathrm{f} + \boldsymbol{f}_\mathrm{adh} + \boldsymbol{f}_\mathrm{cap} + \boldsymbol{f}_\mathrm{pp-cap}, \tag{10}$$

and

$$\bar{\bar{\boldsymbol{I}}}\dot{\boldsymbol{\omega}}_\mathrm{p} = \boldsymbol{T}_\mathrm{c}, \tag{11}$$

where m_p is the mass of the particle, $\boldsymbol{v}_\mathrm{p}$ is the velocity of the particle, and $\boldsymbol{\omega}_\mathrm{p}$ is the rotational velocity of the particle. The first term on the right-hand side of Eq. (10) represents the forces associated with gravitational acceleration $\boldsymbol{g}$, where ρ_p and ρ_f are the densities of the particles and fluid, respectively. $\boldsymbol{f}_\mathrm{c}$ represents the forces acting on the particle arising from particle–particle and particle-substrate interactions, $\boldsymbol{f}_\mathrm{f}$ is the drag force resulting from particle-fluid interactions, $\boldsymbol{f}_\mathrm{adh}$ accounts for the adhesive van der Waals forces between multiple particles, $\boldsymbol{f}_\mathrm{cap}$ represents the capillary force on a particle at the gas-liquid interface, and $\boldsymbol{f}_\mathrm{pp-cap}$ describes the force between two particles at the gas-liquid interface. Eq. (11) defines the rotational acceleration of the particle, where $\bar{\bar{\boldsymbol{I}}}$ is the moment of inertia and $\boldsymbol{T}_\mathrm{c}$ is the sum of external torques acting on the particle due to particle–particle and particle-substrate interactions.

2.2.1. Forces acting on the particles

The interactions between particles and the substrate generate forces that can be modeled using a nonlinear spring-dashpot-slider system. This system is based on the physical characteristics of the particles and the degree of deformation that occurs during their interactions. The total force exerted during a collision is calculated by combining the normal and tangential components,

$$\boldsymbol{f}_\mathrm{c} = \boldsymbol{f}_\mathrm{c,n} + \boldsymbol{f}_\mathrm{c,t}, \tag{12}$$

which are determined using the physical properties of the particles and the extent of their deformation. For a collision with an overlap of δ_n, a relative particle velocity $\boldsymbol{v}_{\mathrm{pp}}$, and a normal contact vector $\boldsymbol{n}$, the normal force is given by Tsuji et al. (1992)

$$\boldsymbol{f}_{\mathrm{c,n}} = \left(K_{\mathrm{n}} \delta_{\mathrm{n}}^{\frac{3}{2}} - \eta_{\mathrm{n}} \boldsymbol{v}_{\mathrm{pp}} \cdot \boldsymbol{n} \right) \boldsymbol{n}, \tag{13}$$

$$K_{\mathrm{n}} = \frac{4R^*}{3E^*}, \tag{14}$$

$$\eta_{\mathrm{n}} = \alpha_{\mathrm{d}} (m^* K_{\mathrm{n}})^{\frac{1}{2}} \delta_{\mathrm{n}}^{\frac{1}{4}}, \tag{15}$$

where R^*, E^* and m^* are the reduced radius, the Young's modulus, and the mass of the particles, respectively, calculated as

$$R^* = \frac{R_1 R_2}{R_1 + R_2} \tag{16}$$

$$E* = \frac{E_1 E_2}{E_1(1+v_2^2) + E_2(1+v_1^2)} \tag{17}$$

$$m = \frac{m_1 m_2}{m_1 + m_2} \tag{18}$$

where the subscripts 1 and 2 indicate each of the two particles considered during their collision. Following Tsuji et al. (1992), the damping coefficient α_{d} is empirically related to the coefficient of restitution of the particle material.

The tangential contact forces resulting from particle–particle and particle-substrate interactions are determined as (Mindlin and Deresiewicz, 1953)

$$\boldsymbol{f}_{\mathrm{c,t}} = \begin{cases} -K_{\mathrm{t}} \boldsymbol{\delta}_{\mathrm{t}} - \eta \cdot \boldsymbol{v}_{\mathrm{s}} & \text{if } |\boldsymbol{f}_{\mathrm{c,t}}| < \mu_{\mathrm{f}} |\boldsymbol{f}_{\mathrm{c,n}}|, \\ \mu_{\mathrm{f}} |\boldsymbol{f}_{\mathrm{c,n}}| \boldsymbol{t} & \text{otherwise,} \end{cases} \tag{19}$$

with the tangential spring constant

$$K_{\mathrm{t}} = 8\sqrt{R^* \delta_{\mathrm{n}}} G^*, \tag{20}$$

where $\boldsymbol{\delta}_{\mathrm{t}}$ denotes the cumulative tangential displacement projected onto the plane perpendicular to the collision normal, $\boldsymbol{v}_{\mathrm{s}}$ denotes the slip velocity between the two particle surfaces at the point of contact, μ_{f} denotes the friction coefficient, $\boldsymbol{t}$ denotes the tangential contact vector (normal to the normal contact vector), and G^* denotes the reduced shear modulus. The tangential spring constant can be directly related to the material properties (Mindlin and Deresiewicz, 1953), where the shear modulus of a particle is calculated from the Young's modulus and the Poisson ratio.

The dominant force acting on a particle from the fluid phase is the drag force, $\boldsymbol{f}_{\mathrm{d}}$, which depends on the relative velocity between the particle and the surrounding fluid. In this work, the drag force is modeled using the expression by Wen and Yu (1966), where the drag force is expressed as

$$\boldsymbol{f}_{\mathrm{d}} = \beta \frac{V_{\mathrm{p}}}{(1-\epsilon_{\mathrm{f}})} (\boldsymbol{v}_{\mathrm{f}} - \boldsymbol{v}_{\mathrm{p}}), \tag{21}$$

where V_{p} is the volume of particle with diameter d_{p}, ϵ_{f} is the local fluid volume fraction, $\boldsymbol{v}_{\mathrm{f}}$ is the velocity of the fluid at the particle, and $\boldsymbol{v}_{\mathrm{p}}$ is the velocity of the particle. β is the momentum transfer coefficient, given as (Wen and Yu, 1966)

$$\beta = C_{\mathrm{d}} \frac{3\epsilon_{\mathrm{f}}(1-\epsilon_{\mathrm{f}})\rho_{\mathrm{f}} |\boldsymbol{v}_{\mathrm{f}} - \boldsymbol{v}_{\mathrm{p}}|}{4d_{\mathrm{p}}} \epsilon_{\mathrm{f}}^{-2.65}. \tag{22}$$

The drag coefficient is defined as

$$C_{\mathrm{d}} = \begin{cases} \dfrac{24}{\epsilon_{\mathrm{f}} \mathrm{Re}} \left(1 - 0.15(\epsilon_{\mathrm{f}} \mathrm{Re})^{0.687}\right) & \text{if } \epsilon_{\mathrm{f}} \mathrm{Re} < 1000, \\ 0.44 & \text{if } \epsilon_{\mathrm{f}} \mathrm{Re} > 1000, \end{cases} \tag{23}$$

based on the particle Reynolds number

$$\mathrm{Re} = \frac{\rho_{\mathrm{f}} d_{\mathrm{p}} |\boldsymbol{v}_{\mathrm{f}} - \boldsymbol{v}_{\mathrm{p}}|}{\mu_{\mathrm{f}}}. \tag{24}$$

The adhesion force due to van der Waals effects between particles as well as between the particles and the substrate is described using the Dejarguin-Muller-Toporov (DMT) model (Derjaguin et al., 1975), with the adhesion force given as

$$\boldsymbol{f}_{\mathrm{adh}} = -2\pi R^* \Delta\gamma \boldsymbol{n}, \tag{25}$$

where $\Delta\gamma$ is the work of adhesion or the energy per unit area required to pull two infinite planar surfaces apart, and $\boldsymbol{n}$ is the normal contact vector. The DMT model offers a straightforward framework to be applied in DEM simulations (Wilson et al., 2016).

The capillary interaction between particles and the interface exerts a force on the particles, as a result of which the particles adsorb at the interface. The capillary force on the particle due to the interface is given as (Lebedev-Stepanov and Vlasov, 2013; Jain et al., 2024)

$$\boldsymbol{f}_{\mathrm{cap}} = \begin{cases} 2\pi r_1 f \, \boldsymbol{n} & \text{if } r_1 < R, \\ \boldsymbol{0} & \text{otherwise,} \end{cases} \tag{26}$$

where r_1 is the distance between the particle center and the interface, R is the radius of the particle, f is the surface free energy or the interfacial tension at the liquid-particle interface, obtained experimentally. The deformation of the surrounding interface causes particles situated on it to generate an inter-particle force, a phenomenon referred to as the "Cheerios effect" (Vella and Mahadevan, 2005). In this study, the force is modeled as a simplified version of the expression proposed by Vassileva et al. (2005), as Li et al. (2011)

$$\boldsymbol{f}_{\mathrm{pp-cap}} = -\pi\sigma \left(\frac{R^{*2}}{2} \sin^2(\beta_0) \tan^2(\alpha_{\mathrm{c}} - \beta_0) \frac{\boldsymbol{n}}{d} \right), \tag{27}$$

where d is the distance between the two particle centers, and β_0 and α_c are the central cone angle of the contact point and contact angle between the fluid and the particle, respectively (Vassileva et al., 2005).

A rotating particle experiences a torque which opposes its rotating motion (van Wachem et al., 2017; Tomas, 2007). The opposing torque is comprised of two components: τ_θ which relates to the total angle rolled, and a dissipative term, τ_d, which is proportional to the angular velocity of rotating and is given by

$$\boldsymbol{\tau}_{\boldsymbol{d}} = -\mu_d |\boldsymbol{f}_{\mathbf{c,n}}| \left(\frac{\boldsymbol{\omega}}{|\boldsymbol{\omega}|} \right), \tag{28}$$

where $\boldsymbol{\omega}$ is the relative angular velocity of the particle and μ_d is the coefficient of rotating friction with units of length. The first component, τ_θ, bears a strong resemblance to the Mindlin-Deresiewicz model of friction (Mindlin and Deresiewicz, 1953). For a two-dimensional system, in each time step the angle rolled between two particles is determined by their respective angular velocities:

$$\Delta\theta_{\mathrm{r}} = \Delta t(\omega_1 - \omega_2) \tag{29}$$

$$\theta_{\mathrm{r}}^n = min(\theta_{\mathrm{r}}^{n-1} + \Delta\theta_{\mathrm{r}}^n, \theta_0) \tag{30}$$

where ω_i is the angular velocity of particle i, and Δt is the time step of integration. The total angle rolled can then be calculated incrementally, by summing the contribution in each time step. Up until a critical angle θ_0, the torque is proportional to θ_{r}. This critical angle is an empirical parameter of the model. If the particle starts to roll back in the opposite direction, *i.e.*, if $\theta_{\mathrm{r}} < 0$, the torque should fall linearly back to 0 such that the particle may roll a distance before coming to a halt. It is therefore useful to limit the magnitude of θ_{r} to θ_0, resulting in the required behavior for τ_θ with no further modification. The torque is thus related to θ_{r} by the relationship

$$\tau_\theta = \begin{cases} -k_{\mathrm{r}} \theta_{\mathrm{r}} & \text{if } |\theta_{\mathrm{r}}| < \theta_0, \\ -\tau_0 \frac{\theta_{\mathrm{r}}}{|\theta_{\mathrm{r}}|} & \text{otherwise,} \end{cases} \tag{31}$$

where k_{r} and τ_0 are proportionality constant given as

$$\tau_0 = \mu_0 R^* f_{\mathrm{c,n}} \tag{32}$$

$$k_{\mathrm{r}} = \frac{\tau_0}{\theta_0}, \tag{33}$$

where μ_0 is the coefficient of rotating resistance, which is an empirical parameter.

2.2.2. Integration of the particle trajectories

Once the forces on each particle are determined, the position vector for every particle is updated at each time interval using the Verlet algorithm (Allen and Tildesley, 1989),

$$\boldsymbol{x}_\mathrm{p}(t+\Delta t) = 2\boldsymbol{x}_\mathrm{p}(t) - \boldsymbol{x}_\mathrm{p}(t-\Delta t) + \Delta t^2 \frac{\boldsymbol{f}_\mathrm{p}(t)}{m_\mathrm{p}} + \mathcal{O}(\Delta t^4), \tag{34}$$

where $\boldsymbol{f}_\mathrm{p}(t)$ is the sum of all forces acting on the particle and Δt is the applied numerical time step. The velocity of the particle is computed as

$$\boldsymbol{v}_\mathrm{p}(t) = \frac{\boldsymbol{x}_\mathrm{p}(t+\Delta t) - \boldsymbol{x}_\mathrm{p}(t-\Delta t)}{2\Delta t} + \mathcal{O}(\Delta t^2). \tag{35}$$

2.3. Numerical procedure

In this study, a two-stage simulation procedure, described in detail in our previous work (Jain et al., 2024), is used. In the first stage, the gas-liquid flow is simulated without accounting for the particles, while in the second stage, the behavior of the bidisperse particles is simulated and analyzed using the results from the gas-liquid flow simulations of the first stage.

In stage 1, the governing equations of the gas-liquid flow are solved using a finite-volume algorithm (Denner and van Wachem, 2014b; Denner et al., 2020), combined with an algebraic VOF method (Denner and van Wachem, 2014a) to capture the gas-liquid interface. In stage 2, the flow data from stage 1 is used to simulate the particle behavior using a Lagrangian particle tracking method. The forces acting on the particles are computed based on the fluid flow and interface properties.

The fluid flow simulations in stage 1 are performed with a time step of $\Delta t = 5\times10^{-6}$ s, with the results stored at intervals of $t_\mathrm{out} = 5\times10^{-4}$ s. In stage 2, the Lagrangian particle-tracking algorithm operates with a smaller time step of $\Delta t = 5\times10^{-8}$ s. The storage interval in stage 1 is chosen such that the interface movement due to evaporation during each time step is significantly smaller than the smallest diameter of the particles.

3. Case setup

This study investigates the dispersion of bidisperse particles in evaporating sessile droplets with a moving contact line, focusing on the roles of surface wettability, Marangoni stresses, and the relative density of the particles compared to the fluid. Ethanol is selected as the solvent for the sessile droplet in all the simulations due to its higher volatility compared to water, which results in a higher evaporation rate (Gurrala et al., 2019). In the first simulation stage, the contact angle is varied and the effect of considering the Marangoni stresses is investigated. In the second stage, also the relative density of the particles compared with the density of the fluid is varied.

3.1. Considered cases

The first stage involves six simulations of depinned ethanol sessile droplet evaporation, with initial contact angles of $\theta = \{60°, 90°, 120°\}$. For each contact angle, two simulations are performed: in one simulation the Marangoni stresses are considered, while in the other simulation the Marangoni stresses are neglected. These six cases are labeled as C1, C2, C3, C4, C5 and C6. Cases C1 and C2 involve a droplet with a contact angle $\theta = 60°$, C3 and C4 involve a droplet with a contact angle $\theta = 90°$, and C5 and C6 involve a droplet with a contact angle $\theta = 120°$. Marangoni stresses are considered in the even-numbered cases and are neglected in the odd-numbered cases. The droplet is placed in air at an ambient pressure of 101325 Pa and an ambient temperature of 25 °C, with the fluid properties detailed in Table 1, and the substrate temperature is kept fixed at $T_\mathrm{s} = 50\,°\mathrm{C}$.

Table 1
Properties of the liquid-gas system (ethanol-air) used for all the simulations in stage 1.

Parameters	Ethanol	Air
Density (kg/m^3)	750	1.23
Viscosity (Pa s)	0.65×10^{-3}	1.78×10^{-5}
Thermal conductivity (W/m K)	0.165	0.046
Specific heat capacity (J/kg K)	2750	1000
Latent heat of vaporization (J/kg)	0.9×10^{6}	–
Molar mass (kg/mol)	0.029	0.046
Boiling temperature (K)	351	–
Surface tension coefficient (N/m)	0.022	–
Temperature coefficient of surface tension (N/m K)	-1.2×10^{-4}	–

Table 2
Properties of the particles used for all the simulations in stage 2.

Parameters	Value
Density (kg/m^3)	2650
Young's modulus (MPa)	1.0
Poisson's ratio	0.15
Friction coefficient	0.3
Coefficient of restitution	0.8
Volume fraction of particles	0.5
Number of particles	607

Table 3
The simulation cases carried out in this work, where C1 - C6 have variation in substrate temperature and in taking into account the Marangoni stresses, or neglecting them. The heavier silica particles are denoted with suffix S and the neutrally buoyant particles are denoted with suffix N.

Stage 1		Stage 2	
Cases	Properties	Cases	Properties
C1	$\theta = 60°$ No Marangoni stresses	C1S C1N	Silica particles Neutrally buoyant particles
C2	$\theta = 60°$ Marangoni stresses	C2S C2N	Silica particles Neutrally buoyant particles
C3	$\theta = 90°$ No Marangoni stresses	C3S	Silica particles
C4	$\theta = 90°$ Marangoni stresses	C4S	Silica particles
C5	$\theta = 120°$ No Marangoni stresses		
C6	$\theta = 120°$ Marangoni stresses		

In the second stage, bidisperse particles with radii $R_\mathrm{p} = \{1.5\ \mu\mathrm{m}, 2.5\ \mu\mathrm{m}\}$ are randomly distributed within the droplet. Particles of both sizes are added until the volume fraction associated with each particle size is 0.1%. The properties of the silica particles simulated in this study are given in Table 2. Using the data from a number of cases from stage 1, simulations with particles are carried out to examine the influence of the contact angle and the Marangoni stresses on the particle dispersion inside the droplet. The two-stage model also enables the examination of the impact of the particle density using the same fluid flow results. In this context, we also evaluate neutrally buoyant particles ($\rho_\mathrm{p} = \rho_\mathrm{f}$), maintaining all properties listed in Table 2, except for the particle density. For the second-stage simulations, case names from the corresponding first-stage simulations are extended with a suffix: standard silica particles are identified by the suffix S, while neutrally buoyant particles are designated with the suffix N. The case names for both the stages are summarized in Table 3.

To analyze the fluid velocity and temperature fields inside the droplet, four specific time instances are discussed below, corresponding to times when 90%, 75%, 50% and 25% of the initial volume of the droplet is left, for three different contact angles.

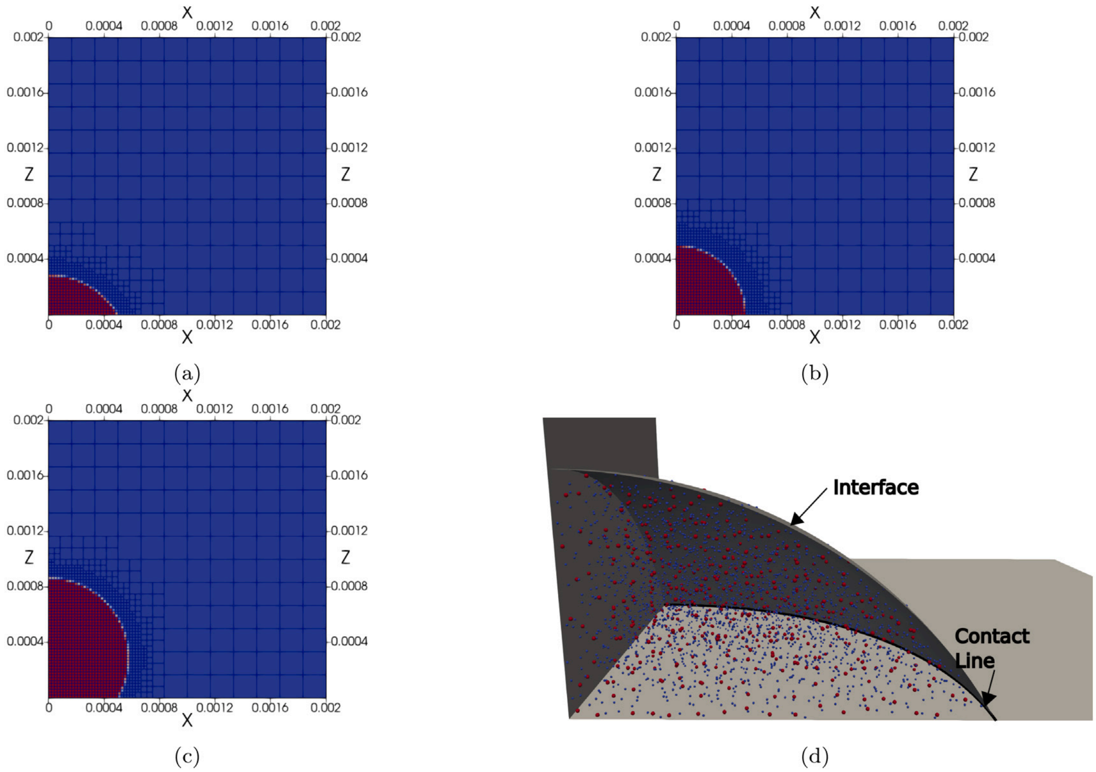

(a) (b)

(c) (d)

Fig. 1. A cross-section of the simulation geometry, showing the mesh refinement near the droplet and the initialization of the color function for stage 1, **(a)** $\theta_c = 60^\circ$ **(b)** $\theta_c = 90^\circ$ **(c)** $\theta_c = 120^\circ$. **(d)** The initialization of bidisperse particles inside the droplet in stage 2. The particle size depicted in the figure is significantly enlarged for visualization purposes.

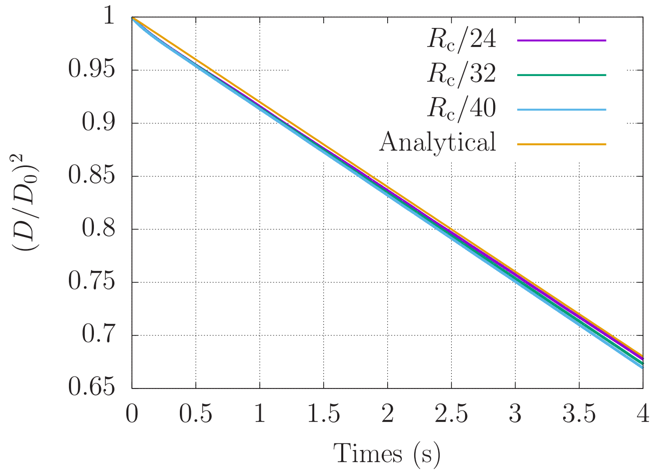

Fig. 2. Validation and mesh sensitivity study for an evaporating droplet with moving contact line, comparing the numerical results of the evaporation of an isothermal sessile droplet with three mesh resolutions against the analytical solution given in Eq. (36).

3.2. Boundary and initial conditions

Given the axisymmetric nature of the evaporation dynamics of a sessile droplet on a heated substrate, only a quarter of the droplet is simulated to create a three-dimensional domain for the particle simulations in stage 2. In stage 1, the lower boundary in the z-direction, *i.e.*, $z = 0$, represents the substrate at a fixed temperature, T_s, a no-slip condition ($\boldsymbol{u} = 0$), and no penetration of the vapor mass, that is, $\boldsymbol{n}_z \cdot \nabla c = 0$. A Neumann-type boundary condition is applied to the liquid volume fraction to facilitate a moving contact line. The movement of contact line has been simulated by regularly re-initializing the droplet, which not only maintains the spherical shape of the droplet but also corrects the position of the contact line. The movement of the contact line has been validated against experimental results as described in Section 4. The study deliberately avoids the prevalent model of contact angle implementation (Afkhami et al., 2009), *i.e.*, by fixing the normals of the interface at the contact line, to avoid the issues of spurious currents. Applying the no-slip boundary condition for a moving contact line may cause a singularity in the stress and a logarithmic singularity in the energy dissipation rate at the contact line. This was first pointed out by Huh and Scriven (1971), and is usually referred to as the Huh-Scriven paradox. However, most interface-capturing techniques, such as the VOF method used in this work, utilize the velocity normal to the mesh faces to advect the volume fraction field, which implies that the methodology includes an "implicit" slip length at the no-slip boundary (Afkhami et al., 2009). To further analyze the effect of different slip lengths, a study of fluid flow and temperature distribution evolution is presented in Appendix B, which suggests that with the given model, the no-slip boundary condition is an adequate choice. This choice of boundary condition is also consistent with other studies simulating sessile droplets with moving contact lines (Paul and Dhar, 2023; Shang et al., 2024; Zhu and Shi, 2021; Zhu et al., 2021). A symmetry boundary condition is used in the lower x- and y-directions, *i.e.*, $x = 0$ and $y = 0$.

Earlier studies opted for a large gas-phase domain Hu and Larson (2002), Chen et al. (2017), typically ranging from 20 to 50 times the droplet radius, using Dirichlet boundary conditions for both temperature and vapor concentration to ensure that the vapor distribution surrounding the droplet was not influenced by the far-field boundary conditions. To reduce the size of the computational domain without adversely impacting the simulation results, the assumption of a diffusion-dominated distribution of the vapor concentration and temperature in the gas away from the interface ($\Delta c = 0$ and $\Delta T = 0$) is employed (Diddens et al., 2017). For the vapor concentration and the temperature, boundary conditions at the upper limits of the domain ($x, y, z = L$, where L represents the domain size) are established by

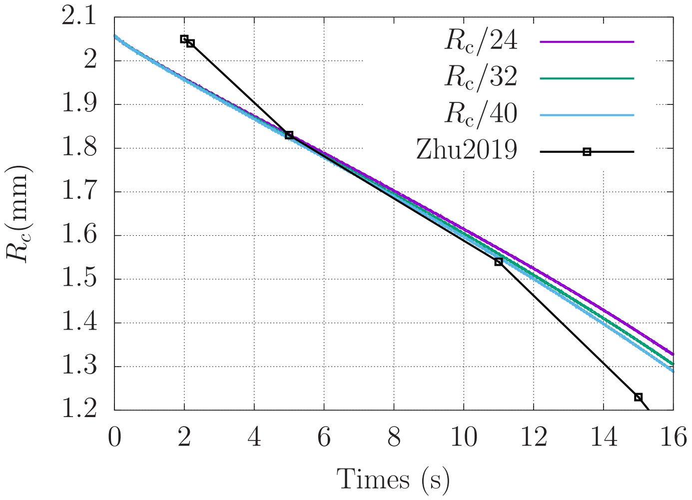

Fig. 3. Validation and mesh sensitivity study for the n-hexane evaporating droplet, comparing the numerical results of the contact radius evolution with three mesh resolutions with the experimental solution given by Zhu and Shi (2019).

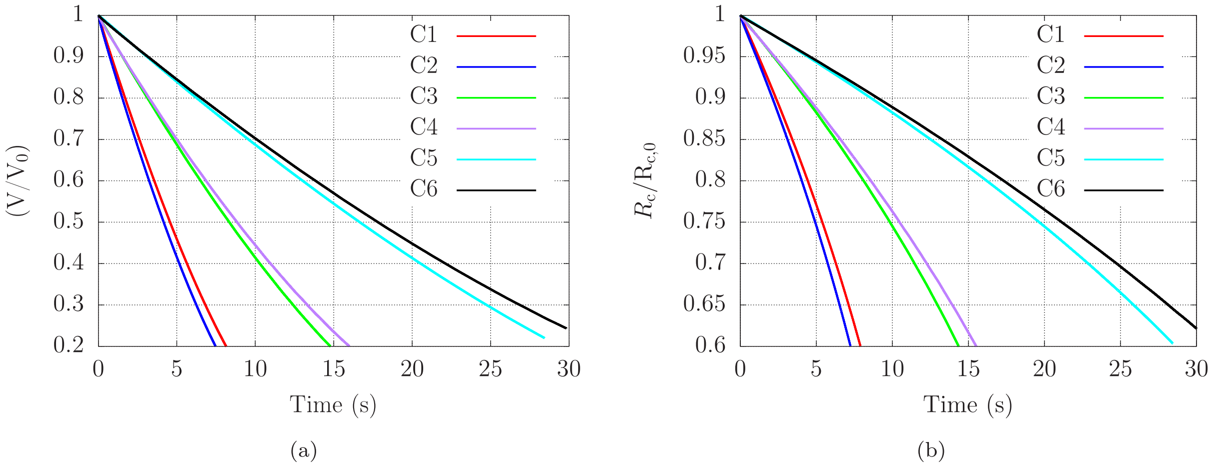

Fig. 4. The simulated normalized droplet volume **(a)** and the contact radius of the droplet **(b)** as a function of time for all 6 cases.

assuming a constant gradient of values perpendicular to the boundary. The vapor concentration field is obtained by solving the Laplace equation. This approach enables the reduction of the domain size to four times the droplet contact radius ($L = 4R_c$), as confirmed in Section 4.

The computational cost is further reduced by using an adaptively refined mesh in and around the droplet to simulate the flow in stage 1, as shown in Figs. 1(a)-1(c). For the initialization of the droplet, the liquid volume fraction and vapor concentration are initialized as a spherical cap. Inside the droplet, the liquid volume fraction is 1 and the vapor mass concentration is the liquid density (Zanutto et al., 2022). The initial temperature and velocity are set to 25 °C and 0, respectively, throughout the domain and the pressure is set to atmospheric pressure. In stage 2, bidisperse particles are randomly placed inside the droplet as shown in Fig. 1(d).

4. Validation

Various aspects of the employed model have been extensively validated in our previous study (Jain et al., 2024). We validate the model for the evaporation of a sessile droplet with a moving contact line using the analytical solution of the volume evolution during the evaporation of an isothermal sessile droplet with a contact angle of 90° (Erbil, 2012). Fig. 2 shows a comparison between the numerical results of the volume evolution of an isothermal sessile droplet with a moving contact line and with an initial contact angle of $\theta = 90°$ and the analytical solution,

$$D^2_{\text{droplet,i}} - D^2_{\text{droplet}} = \frac{8D(c_s - c_\infty)}{\rho_l} t, \tag{36}$$

where c_s is the vapor concentration at the sphere surface, c_∞ is the vapor concentration at infinity, $D_{\text{droplet,i}}$ is the initial diameter of the spherical droplet, and D_{droplet} is the instantaneous droplet diameter. The sensitivity of the results with respect to the mesh resolution is assessed using three different mesh resolutions, where the initial contact radius of the droplet is resolved by 24, 32 and 40 cells. As depicted in Fig. 2, the results from all the numerical resolutions agree well with the analytical solution, demonstrating that the results from stage 1 are independent of the mesh resolution.

Further validation of the model is carried out with the experimental results of Zhu and Shi (2019), wherein an n-hexane droplet evaporating in CCA mode with contact angle $\theta_c = 27.47°$ and initial contact radius $R_c = 2.1$ mm on a heated substrate with $T_s = 35.33$ °C is considered. Fig. 3 shows the evolution of the contact radius predicted by the simulations at three different resolutions, compared against the experimental measurements of Zhu and Shi (2019). The simulation results are in good agreement with the experimental results. Thus, for subsequent analyses, the lower mesh resolution, where the contact radius is resolved by 24 cells, is used. To validate the mesh independence of the fluid flow in the presence of Marangoni stresses, case C4 is simulated with different

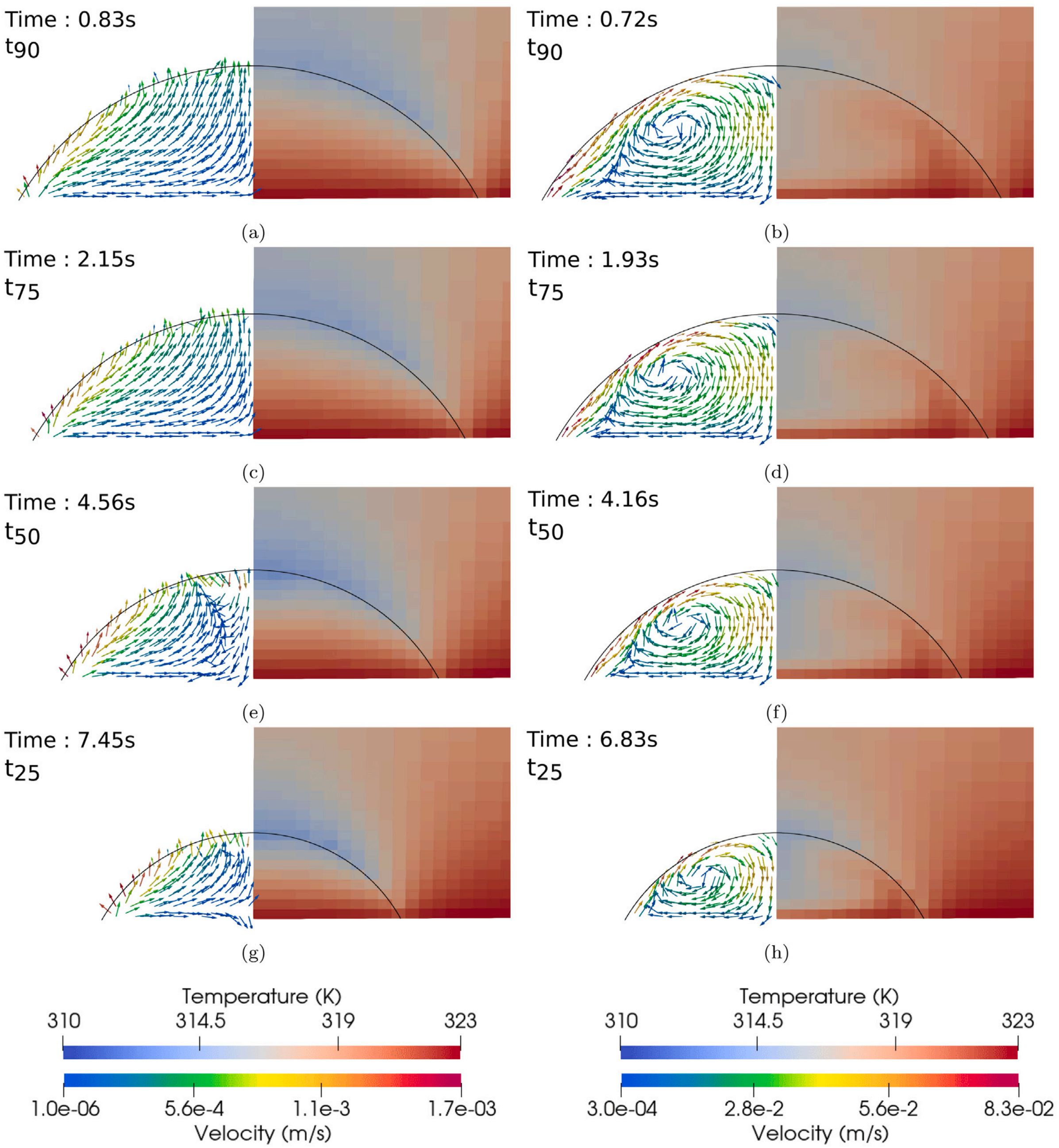

Fig. 5. Velocity vectors and temperature plots at four different time instances of the cases with a contact angle of $\theta_c = 60°$ without taking into account the Marangoni stresses, C1 (left column), and with Marangoni stresses, C2 (right column). Velocity vector plots are shown on the left, where the color indicates the velocity magnitude. Contour plots of the temperature are shown on the right. **(a)** C1, t_{90}, **(c)** C1, t_{75}, **(e)** C1, t_{50}, **(g)** C1, t_{25}. **(b)** C2, t_{90}, **(d)** C2, t_{75}, **(f)** C2, t_{50}, **(h)** C2, t_{25}.

mesh resolution, where the contact angle is $\theta_c = 90°$ and Marangoni flow is present. The results, presented in Appendix A, demonstrate that the flow is independent of the mesh resolution even in the presence of Marangoni stresses. The validation of the volume evolution through these analytical solutions, and of the contact radius evolution through experimental results, indirectly confirms the accuracy of the velocity and temperature fields, since the velocity, temperature, and species distributions collectively govern the droplet's evaporation dynamics. Furthermore, this study is focussed on the role of Marangoni stresses, which has been validated in our previous work (Jain et al., 2024).

5. Results of stage 1: Flow inside the droplet

In the first stage of this study, the focus is on analyzing the evolution of the contact radius and the fluid flow inside the droplet, as well as the spatial distribution of the temperature and vapor concentration. The temporal evolution of the droplet volume, normalized by the initial droplet volume, is shown in Fig. 4(a). It is observed that increasing the contact angle results in a lower evaporation rate, resulting from the larger initial droplet volume. The presence of Marangoni flow enhances the evaporation rate for cases C1 and C2 ($\theta_c = 60°$), whereas it reduces the evaporation rate for cases C3-C6 ($\theta_c = \{90°, 120°\}$). The evolution of the contact radius is shown in Fig. 4(b), exhibiting an almost linear reduction and a trend similar to the volume of the droplet.

5.1. *Contact angle of* $\theta_c = 60°$

For case C1, where the contact angle is $\theta_c = 60°$ and the Marangoni stresses are neglected, the figures showing the velocity on the left and the temperature distribution inside the droplet on the right are

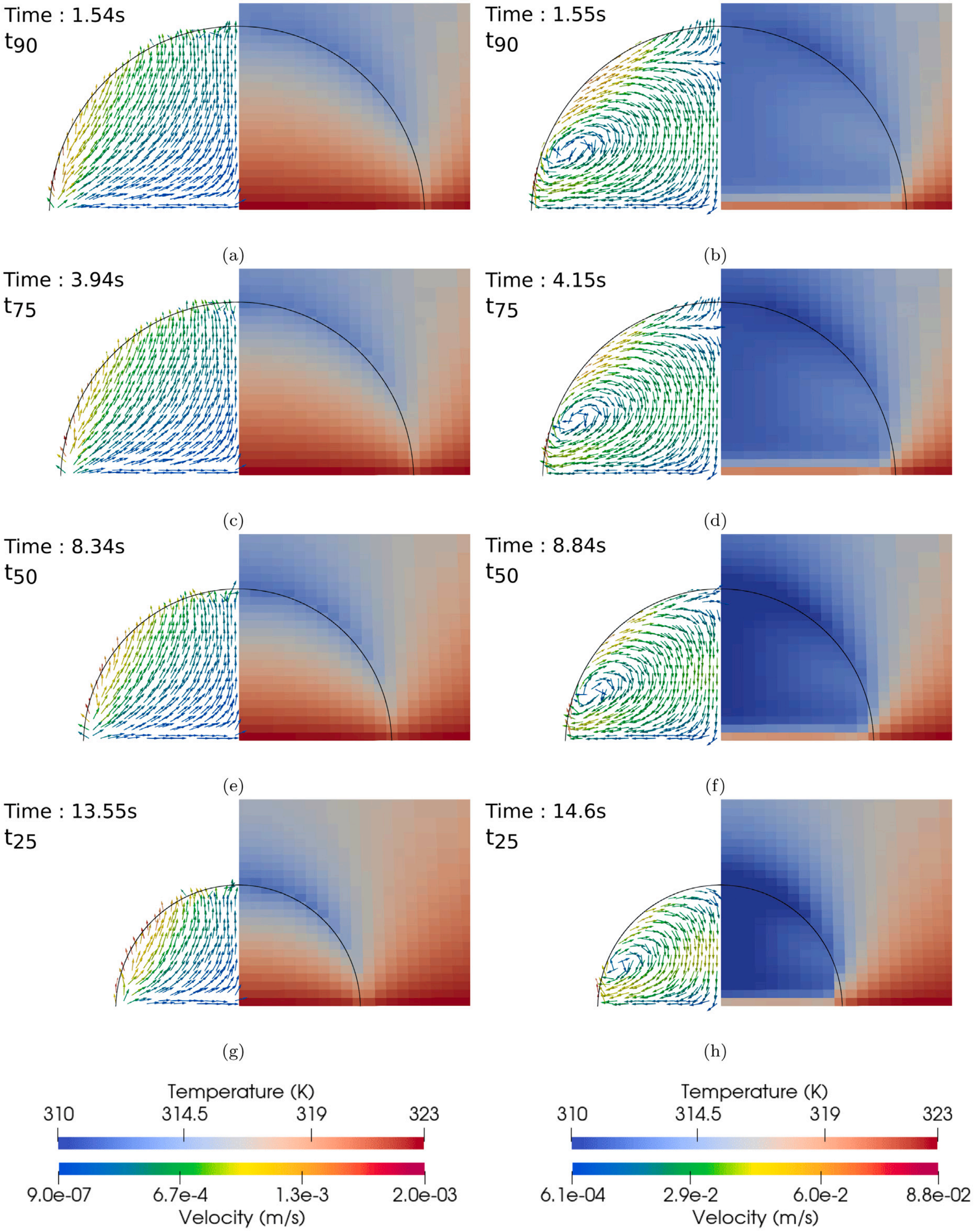

Fig. 6. Velocity vectors and temperature plots at four different time instances of the cases with contact angle $\theta_c = 90°$ without taking into account the Marangoni stresses, C3 (left column), and with Marangoni stresses, C4 (right column). Velocity vector plots are shown on left, where the color indicates the velocity magnitude. Contour plots of the temperature are shown on the right. **(a)** C3, t_{90}, **(c)** C3, t_{75}, **(e)** C3, t_{50}, **(g)** C3, t_{25}. **(b)** C4, t_{90}, **(d)** C4, t_{75}, **(f)** C4, t_{50}, **(h)** C4, t_{25}.

presented for four different time instances in Figs. 5(a), 5(c), 5(e), and 5(g). The development of the fluid flow inside the droplet is determined by solving the continuity and momentum conservation equations, and is a complex interplay of evaporation dynamics, contact line movement and the effect of the Marangoni stresses. A return flow or vortex development inside a droplet is only seen in the case when the Marangoni stresses are present, whereas for the case of capillary flow and the flow induced by the moving contact line a return flow inside the droplet is absent. The receding motion of the contact line pushes the fluid from the contact line to apex of the droplet, opposite to the capillary effect of fluid traveling from apex to the contact line to account for the evaporated liquid at the contact line. A flow from the contact line to the apex of the droplet is observed, which is different from the well-known capillary flow pattern (Hu and Larson, 2005;

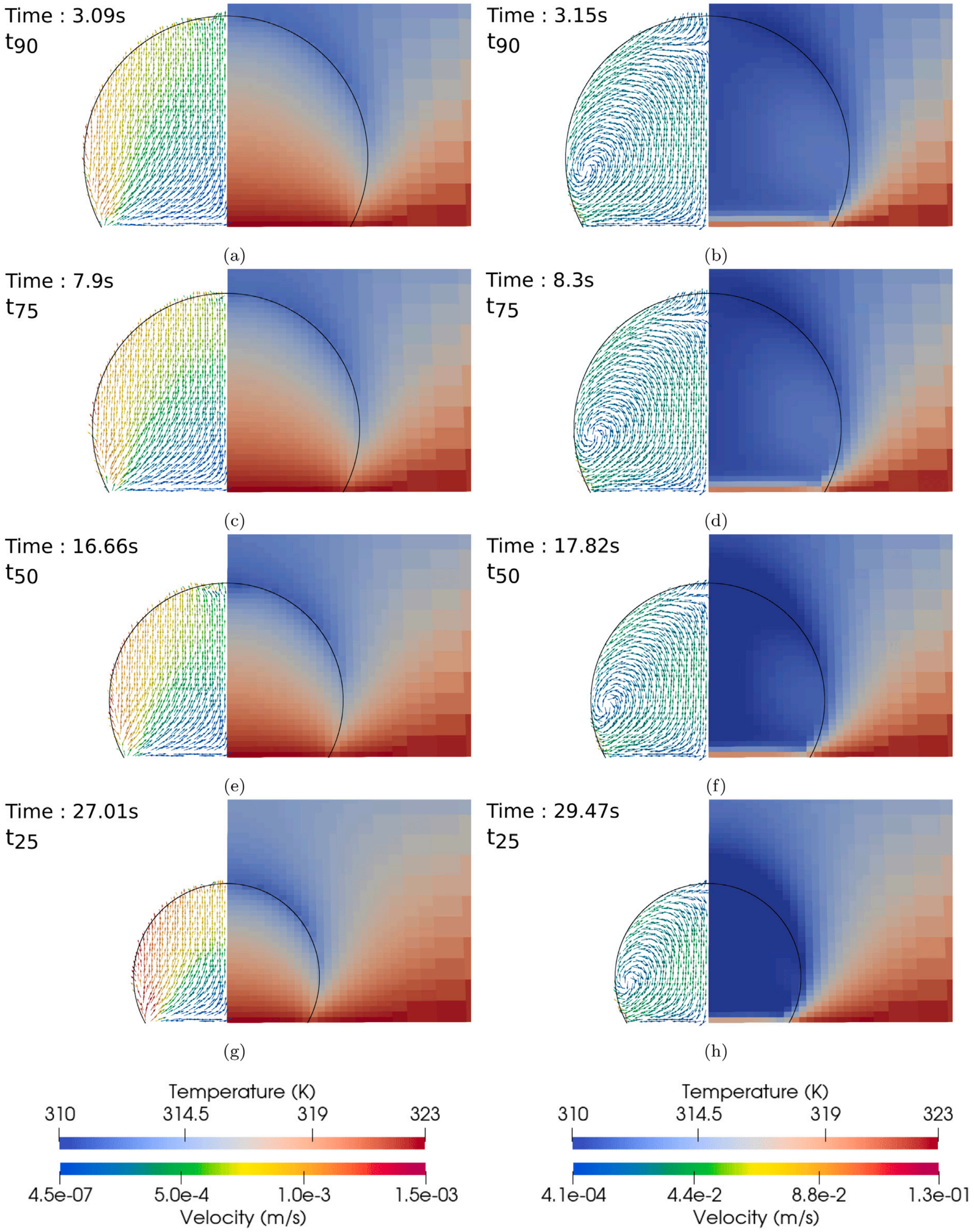

Fig. 7. Velocity vectors and temperature plots at four different time instances of the cases with contact angle $\theta_c = 120°$ without taking into account the Marangoni stresses, C5 (left column), and with Marangoni stresses, C6 (right column). Velocity vector plots are shown on the left, where the color indicates the velocity magnitude. Contour plots of the temperature on shown on the right. **(a)** C5, t_{90}, **(c)** C5 t_{75}, **(e)** C5, t_{50}, **(g)** C5, t_{25}. **(b)** C6, t_{90}, **(d)** C6, t_{75}, **(f)** C6, t_{50}, **(h)** C6, t_{25}.

Barmi and Meinhart, 2014) observed in the absence of Marangoni flow in pinned droplets, with fluid flowing from the apex of the droplet towards the contact line. The fluid motion from the contact line towards the apex of the droplet is attributed to the movement of the contact line. This inference is supported by comparison with a previous study on pinned ethanol droplet evaporation, in which, under the absence of Marangoni stresses, only capillary-driven flow from the apex to the contact line is observed in order to maintain a constant contact radius (Jain et al., 2024). The competing effects of capillary flow and contact-line-induced flow are clearly visualized in Fig. 5(h), where a portion of the liquid is seen moving from the apex towards the contact line, while another portion moves in the opposite direction, from the contact line towards the apex. As evaporation continues and the contact radius decreases, the flow from the contact line to the apex remains

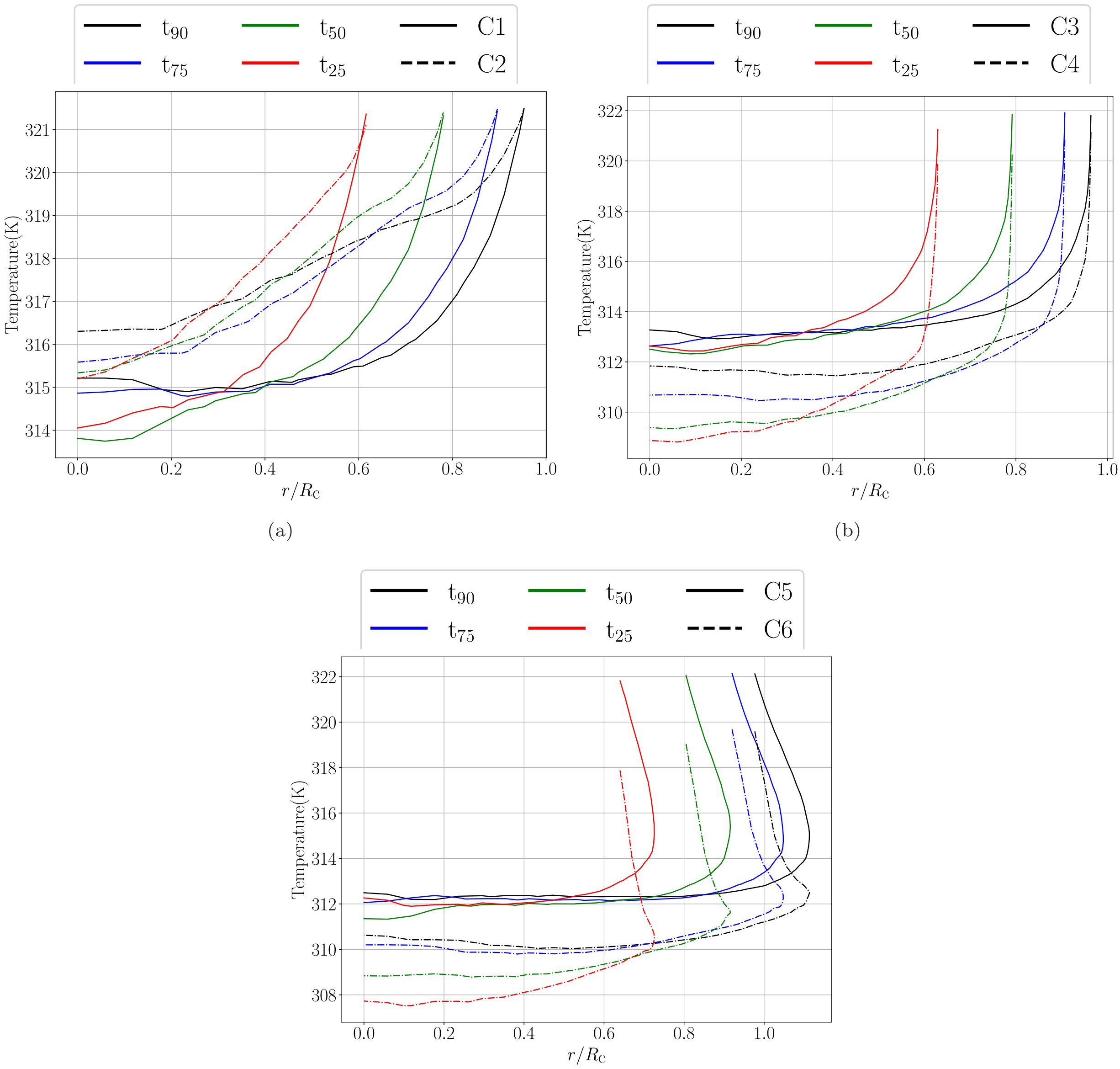

(a)

(b)

(c)

Fig. 8. Temperature distribution along the interface for different time instances. **(a)** $\theta_c = 60°$, neglecting the Marangoni stresses, C1 (solid lines), and including the Marangoni stresses, C2 (dashed lines). **(b)** $\theta_c = 90°$, neglecting the Marangoni stresses, C3 (solid lines), and including the Marangoni stresses, C4 (dashed lines). **(c)** $\theta_c = 120°$, neglecting the Marangoni stresses, C5 (solid lines), and including the Marangoni stresses, C6 (dashed lines).

consistent, with a higher velocity magnitude near the contact line and along the interface compared to the interior bulk of the droplet. The temperature distribution on the right shows that the temperature along the interface increases towards the contact line. The velocity and temperature distributions inside the droplet for case C2, where the contact angle is $\theta_c = 60°$ and the Marangoni stresses are taken into account, are presented in Figs. 5(b), 5(d), 5(f), and 5(h). The flow velocity inside the droplet has a magnitude that is approximately ten times larger than that in case C1 (in which the Marangoni stresses neglected), driven by the Marangoni stresses. The Marangoni stresses move the liquid from the contact line to the apex of the droplet along the interface, forming a vortex inside the droplet. As evaporation continues and the contact radius decreases, the influence of the Marangoni flow reduces as the temperature difference along the interface reduces. A stagnation point is formed at the base of the droplet, which is slightly offset from the contact line. This is a result of the Marangoni flow pushing the liquid inside the droplet, whereas the opposing capillary flow pushes the liquid outward towards the contact line. As the evaporation progresses, the distance of the offset from the contact line decreases. The results in Fig. 5 show that, as a result of Marangoni flow, the temperature of the liquid in case C2 is larger along the interface near the contact line than in the droplet center.

5.2. Contact angle of $\theta_c = 90°$

In Fig. 6, similar plots as in the previous section are shown for cases C3 and C4, for four different time instances, in which the contact angles are $\theta_c = 90°$. The figures showing the fluid velocity field for case C3, where the Marangoni stresses are absent, show similar flow patterns as for case C1; the fluid flows from the contact line to the apex of the droplet and the magnitude of the flow remains approximately constant. In addition, the temperature profiles observed in case C3 show a consistent distribution over time, with the lowest temperature at the apex of the droplet and a higher temperature in the interior of the droplet than near the interface.

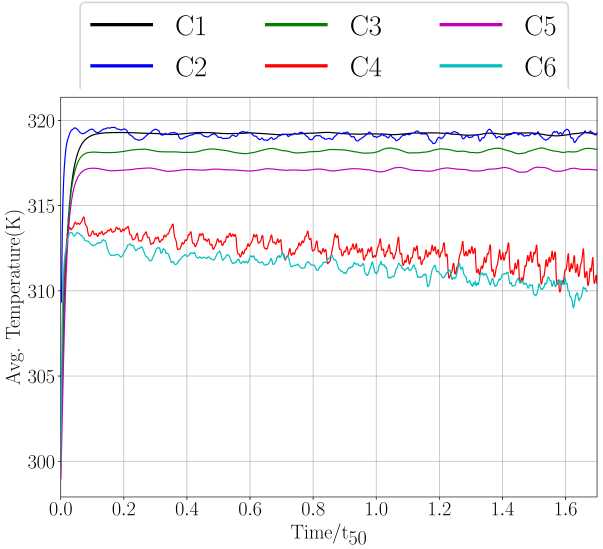

Fig. 9. Evolution of the average temperature of the droplet for all the 6 cases. Time is normalized by the time when half of the droplet has evaporated.

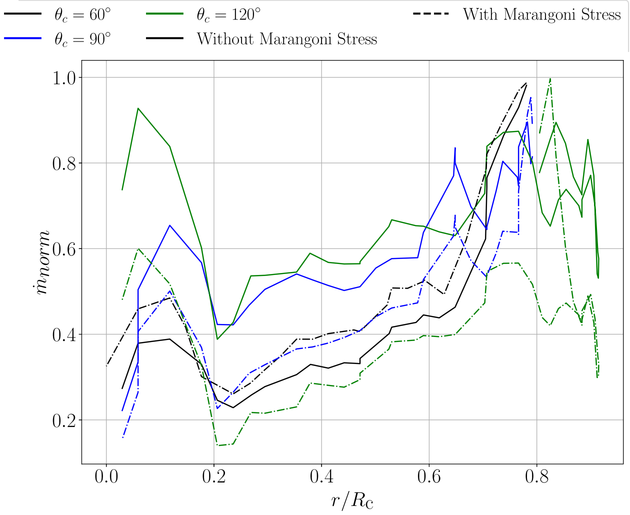

Fig. 10. Localized evaporative mass flux when the droplet has reached 50% of its initial volume for all 6 cases. The solid lines represent the cases where Marangoni stress is included and dashed lines are for cases without Marangoni stresses.

The figure showing the velocity field for the first depicted time instance for case C4 (Fig. 6(b)), shows that the Marangoni flow is stronger than the capillary flow and the flow induced by the receding contact line, resulting in a branching of the flow. A part of the flow moves towards the bottom bulk of the droplet, while the other part moves towards the apex of the droplet. This branching effect of the Marangoni flow is absent in the case of smaller contact angle in case C2, as seen in Fig. 5(b). As the evaporation progresses, the magnitude of the Marangoni stresses and the resulting magnitude of the Marangoni flow reduce as a result of the decreasing temperature difference along the interface. Unlike in case C2, the vortex formed by the Marangoni flow is much closer to the contact line of the droplet and does not exhibit a stagnation point near the substrate.

The figures showing the temperature for case C4 shows a lower temperature at the apex of the droplet than the bulk of the droplet owing to evaporative cooling. The Marangoni flow enhances convective heat transfer and mixing considerably, increasing the temperature along the interface compared to the bulk of the droplet. Contrary to case C2, the temperature in the bulk of the droplet decreases, as evaporative cooling dominates, and the Marangoni-driven convective mixing affects the heat transfer. This is due to the fact that for a droplet with larger contact angle, the thermal resistance is higher and the solid–liquid contact area is smaller.

5.3. Contact angle of $\theta_c = 120°$

Fig. 7 shows the velocity and temperature fields for cases C5 and C6, at four different time instances, in which the contact angles are $\theta_c = 120°$. The figures showing the fluid velocity for case C5, where the Marangoni stresses are absent, show similar flow patterns as are observed in case C3. The fluid flows from the contact line to the apex of the droplet. However, the magnitude of the fluid flow increases during the course of the evaporation process. In addition, the temperature distribution of case C5 exhibits a monotonic distribution along the interface, with the lowest temperature at the apex of the droplet. The temperature in the interior of the droplet is higher than in the proximity of the interface, similar as is observed in cases C1 and C3.

Comparing the velocity fields of cases C5 and C6 suggests that the Marangoni flow is stronger than the capillary flow and the flow induced by the receding contact line, resulting in a branching of the flow in case C6, similar to the branching observed in case C4. The vortex formed by the Marangoni flow is close to the interface and does not show any stagnation point near the substrate. The temperature distribution in case C6 is similar in nature to case C4, showing a lower temperature at the apex of the droplet as a result of evaporative cooling and the large distance of the apex from the heated substrate.

5.4. Discussion

Marangoni stresses play a crucial role for the fluid flow and temperature distribution inside the droplet. For cases in which the Marangoni stresses are neglected, irrespective of the contact angle, the flow induced by the moving contact line dominates the capillary flow, with the fluid flowing from the contact line to the apex of the droplet. This stands in contrast to the explanation provided by Bhardwaj (2018), in which it is suggested that the fluid flows from the contact line to the apex of droplets with moving contact if the contact angle is $\theta_c > 90°$. Bhardwaj (2018) also suggests that the evaporation at the apex of the droplet is higher than at the contact line. However, our results demonstrate that, irrespective of the contact angle, the flow inside a droplet resting on the heated substrate and evaporating in the CCA mode is dominated by the contact line motion rather than by evaporation. If Marangoni stresses are present, the flow induced by these Marangoni stresses dominates the flow inside the droplet, leading to a classical single-vortex flow. The velocity field in a pinned water droplet is studied in Kazemi et al. (2021), and a mathematical model is shown to overpredict the results relative to the experimental measurements. However, to the best of our knowledge, experimental data for the internal velocity field in an ethanol droplet evaporating under constant contact angle conditions are not available in the literature. As a result, the predictive accuracy of the present model under such conditions cannot be directly assessed. Nevertheless, the implementation of Marangoni stresses in the model is independently validated against analytical solutions to ensure physical consistency and to avoid unphysical results.

The temperature distribution along the interface is shown in Fig. 8. Fig. 8(a) shows the interface temperature for cases C1 and C2, where the contact angle is 60°. The interface temperatures are shown for four different time instances with droplet volumes of 90%, 75%, 50%, and 25% of the initial volume of the droplet. For case C1, in which the Marangoni stresses are neglected, the interface temperatures are lower compared to those in case C2, which takes into account the Marangoni stresses. This suggests that the convective mixing due to Marangoni flow increases the interface temperature. Fig. 8(b) illustrates

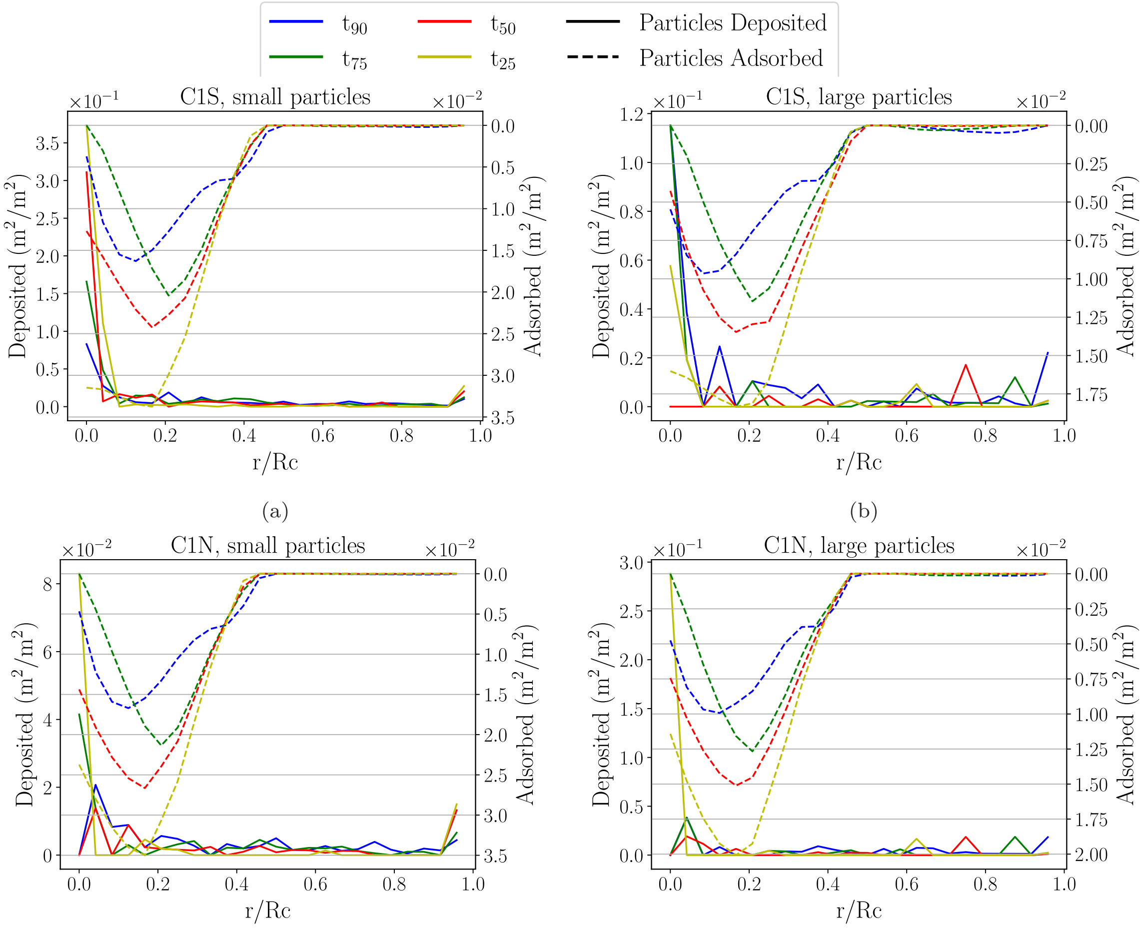

(a) (b)

(c) (d)

Fig. 11. Evolution of surface concentration of particles adsorbed at the interface (dashed lines, right y-axes) and deposited at the substrate (solid lines, left y-axes), for cases without the Marangoni stresses and the contact angle $\theta_c = 60°$. **(a)** Small silica particles of case C1S, **(b)** large silica particles of case C1S, **(c)** small neutrally buoyant particles of case C1N, and **(d)** large neutrally buoyant particles of case C1N.

the interface temperature for cases C3 and C4, where the contact angle is 90°. The overall interface temperature for case C4, considering the effect of the Marangoni stresses, is lower than that for case C3, where the effect of the Marangoni stresses is neglected, unlike the cases where the contact angle is 60°. In case C3, the interface temperature converges towards a constant value at the apex. However, for case C4, the temperature at the apex continuously decreases, with a lower temperature than in case C3. Similar results are obtained for cases C5 and C6, shown in Fig. 8(c), where the presence of Marangoni stresses result in a lower interface temperature in case C6 compared to the interface temperature of case C5. In addition, the apex temperature continuously decreases in case C6, whereas in case C5, the interface region near the apex maintains a constant temperature.

Further analysis of the average temperature of the droplet accounting for both the bulk and interface temperatures is shown in Fig. 9. In cases C1 and C2, where the contact angle is 60°, the average temperature reaches almost the same equilibrium temperature and is maintained for the later stages of evaporation. In case C2, the equilibrium temperature is reached earlier than in the case without Marangoni stress, case C1, due to effective thermal mixing. For cases in which Marangoni stresses are absent and where the contact angles are 90° and 120°, the droplet reaches an equilibrium temperature and maintains it for the later stages of the evaporation process. For cases without Marangoni stresses, droplets with larger contact angles exhibit smaller average temperatures, owing to a higher thermal resistance and a smaller solid–liquid contact area. For cases with Marangoni stresses and contact angles 90° and 120°, the average temperature of the droplet decreased over time, with case C6 having a comparatively lower average temperature than case C4. This is due to the fact that as the evaporation progresses, the solid–liquid contact area decreases. Thus, evaporative cooling dominates for droplets with contact angles $\theta_c \geq 90°$ for cases with Marangoni stresses. Similar observations were reported by Paul and Dhar (2023), where the authors numerically showed that for water droplets evaporating in a depinned state with the Marangoni flow, the evaporative cooling dominates for large contact angles, leading to a smaller average temperature of the droplet.

The localized evaporative mass flux along the droplet interface is presented in Fig. 10 for all cases, corresponding to the moment when the droplet volume has decreased to 50% of its initial value. Cases C1 and C2, characterized by a contact angle of $\theta_c = 60°$ and shown by black lines, exhibit a maximum mass flux near the contact line due to the influence of the heated substrate. Additionally, a local maximum is observed near the apex of the droplet. For cases C3 and C4, shown by blue lines, a similar behavior is observed: the mass flux peaks near the contact line and a secondary local maximum is present near the apex. In cases C5 and C6, indicated by green lines, the distribution of mass flux varies depending on the presence of Marangoni stresses. For the case without Marangoni stress (C5), the maximum mass flux occurs at the apex, with a local maximum near the contact line. In contrast, for the case with Marangoni stress (C6), the maximum mass flux is located at the contact line, with a local maximum near the apex. The local maximum near the apex, observed in all cases, drives an internal flow

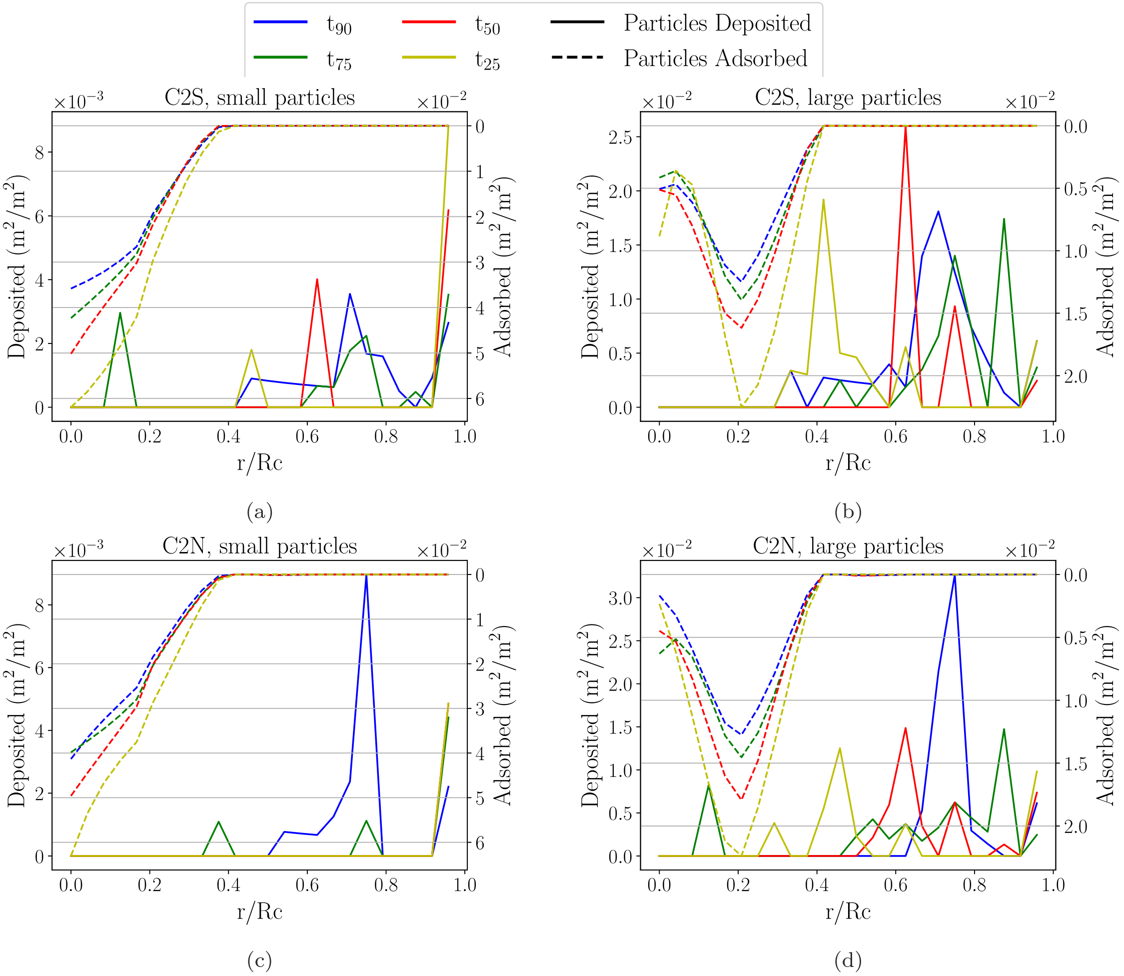

(a)

(b)

(c)

(d)

Fig. 12. Evolution of surface concentration of particles adsorbed at the interface (dashed lines, right y-axes) and deposited at the substrate (solid lines, left y-axes) for cases with the Marangoni stresses and the contact angle $\theta_c = 60°$. **(a)** smaller silica particles of case C2S **(b)** larger silica particles of case C2S **(c)** smaller neutrally buoyant particles of case C2N **(d)** larger neutrally buoyant particles of case C2N.

from the contact line towards the apex, contributing to the maintenance of the droplet's spherical cap shape.

6. Results of stage 2: Dispersion of particles in the evaporating droplet

In the second simulation stage, multiple simulations with particles are carried out based on the flow fields resulting from the simulations carried out in stage 1. The location of the particles is analyzed for four different time instances, corresponding to the volume of the droplet left being 90%, 75%, 50% and 25% of the initial volume of the droplet, for three different contact angles.

6.1. Contact angle of $\theta_c = 60°$

In Fig. 11, the surface concentrations of the small and the large particles that are adsorbed at the interface or deposited on the substrate are shown for case C1, where the contact angle is 60° and Marangoni stresses are absent. Figs. 11(a) and 11(b) show the surface concentrations of silica particles, Figs. 11(c) and 11(d) show the surface concentrations of neutrally buoyant particles. Both the small and the large particles occupy the central region of the droplet, whether they are deposited on the substrate or adsorbed at the interface. For the small particles, the surface concentration of the deposited particles is nearly three times larger than for the larger particles. We attribute this preferential deposition of small particles to the stronger influence of the adhesive van der Waals forces. In addition, the surface concentration for the small particles adsorbed at the interface is nearly double the surface concentration of the large particles. The concentration of particles of both sizes gradually increases at the droplet apex. Similar observations can be made for both types of particles with the same density as the fluid, shown in Figs. 11(c) and 11(d). The only visible difference is that the surface concentration of the neutrally buoyant particles deposited on the substrate is higher for the large particles than for the small particles. The positions of both the small and the large particles are at the same location, suggesting that no significant segregation is seen.

Similar plots are shown in Fig. 12 for the surface concentrations of smaller and larger particles that are adsorbed and deposited in droplet in case C2, where the contact angle is 60° and the Marangoni stresses are taken into account. The small particles adsorbed at the interface of the droplet move towards the apex of the droplet forming a core, as observed in Figs. 12(a) and 12(b), while the larger particles are adsorbed around the core of the smaller particles. As the evaporation progresses, the concentration of particles adsorbed at the interface increases, and the segregation of the small and large particles becomes more prominent. The small particles are deposited on the substrate mostly near the stagnation point, which moves towards the center of the droplet as evaporation progresses. The surface concentration of the large particles on the substrate is nearly three times larger than the surface concentration of the small particles, and it can be seen that the majority of the large particles are deposited at the stagnation

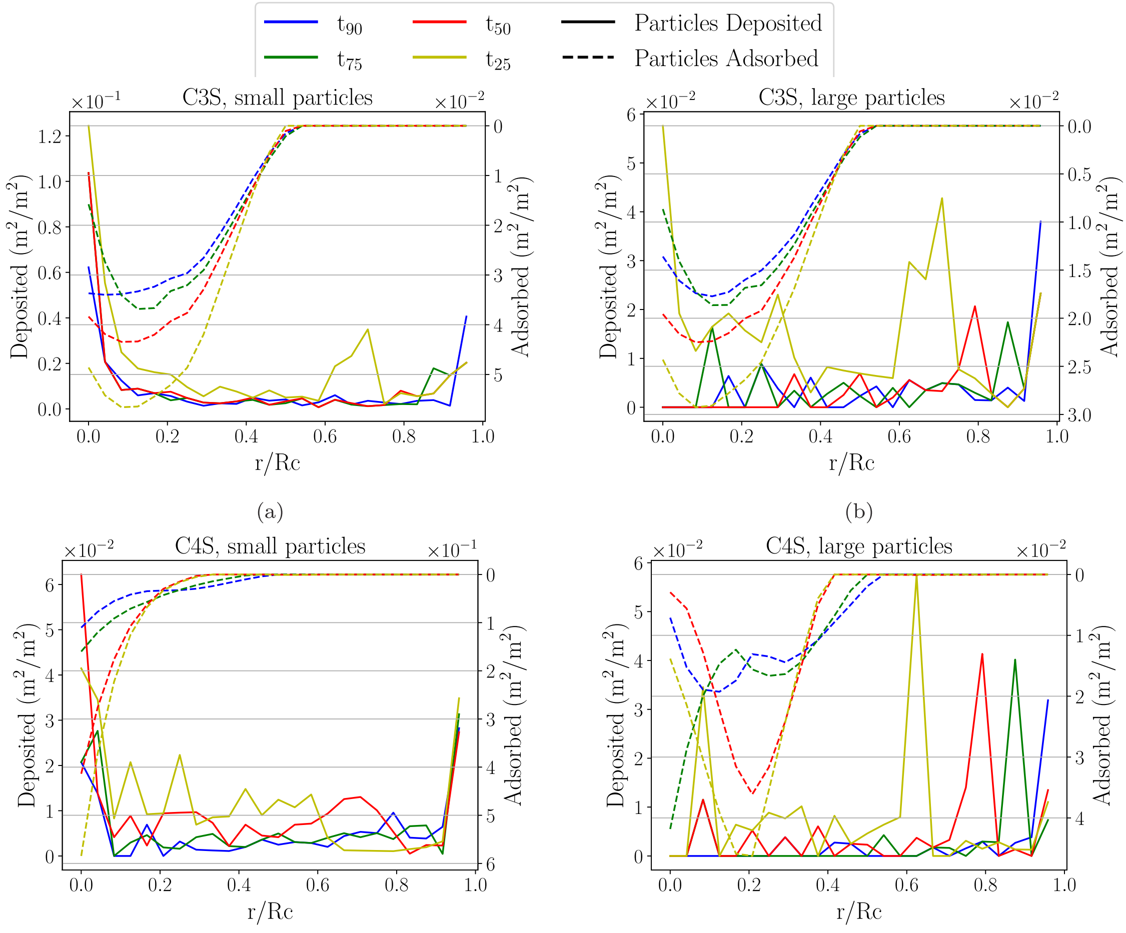

(a) (b)

(c) (d)

Fig. 13. Evolution of surface concentration of particles adsorbed at the interface (dashed lines, right *y*-axes) and deposited at the substrate (solid lines, left *y*-axes), for cases with the contact angle $\theta_c = 90°$. **(a)** Small silica particles of case C3S, **(b)** large silica particles of case C3S, **(c)** small neutrally buoyant particles of case C4S, and **(d)** large neutrally buoyant particles of case C4S.

point, which later moves towards the center of the droplet. Similar observations can be made for both types of particles with the same density as the fluid of the droplet, as shown in Figs. 12(c) and 12(d).

Overall, we can summarize that the trend of particle adsorption and deposition is mostly affected by the presence of the Marangoni flow. In the presence of Marangoni flow, we observe a separation of small and large particles. The density of particles relative to the density of the fluid has, however, no significant influence.

6.2. *Contact angle of $\theta_c = 90°$*

Fig. 13 shows the results of the deposition and adsorption of the silica particle for cases C3 and C4, where the contact angle is 90° and Marangoni stresses are absent and present, respectively. Comparing the plots in Figs. 13(a) and 13(b) for case C3, where the Marangoni flow is absent and the fluid flows from the contact line to the apex of the droplet, both the small and the large particles are adsorbed at the apex of the droplet, where the surface concentration gradually increases. For the small particles that are deposited on the substrate, the surface concentration is higher at the center of the droplet for all four shown time instances. On the other hand, the large particles are only deposited near the contact line, which gradually moves towards the center of the droplet.

Figs. 13(c) and 13(d) shows the positions of the particles for case C4, where the Marangoni flow is present. A arrangement of particles similar to the one seen for case C2 can be observed in Figs. 13(c) and 13(d) for case C4: The small particles adsorbed at the apex of the droplet form a core and the large particles adsorbed at the interface surround the core of the small particles. The surface concentration of the adsorbed particles gradually increases as the evaporation proceeds. For the deposited particles, small particles are mainly found at the center of the droplet. In contrast, the large particles primarily occupy the region near the contact line and a few large particles surround the core of the small particles deposited on the substrate.

Overall, we see a similar scenario for cases C3 and C4 as for cases C1 and C2, where the Marangoni flow has a significant effect on the segregation of the small and large particles, with small particles moving towards the center, where they form a core of adsorbed and deposited particles, and the large particles surround them.

6.3. *Self-sorting mechanisms*

In most cases considered in this study, the particles classify at the interface; the smaller particles are sorted from the larger ones. This self-sorting of the particles in an evaporating sessile droplet is governed by the flow inside the droplet. For a sessile droplet with a moving contact line, three types of flow together form the resulting fluid flow: (i) the flow induced by the moving contact line, (ii) the capillary flow, generated by evaporation, and (iii) the Marangoni flow, generated by the Marangoni stresses associated with a local change in surface tension due to the temperature gradient along the interface. While the capillary flow moves fluid from the apex of the droplet to the contact

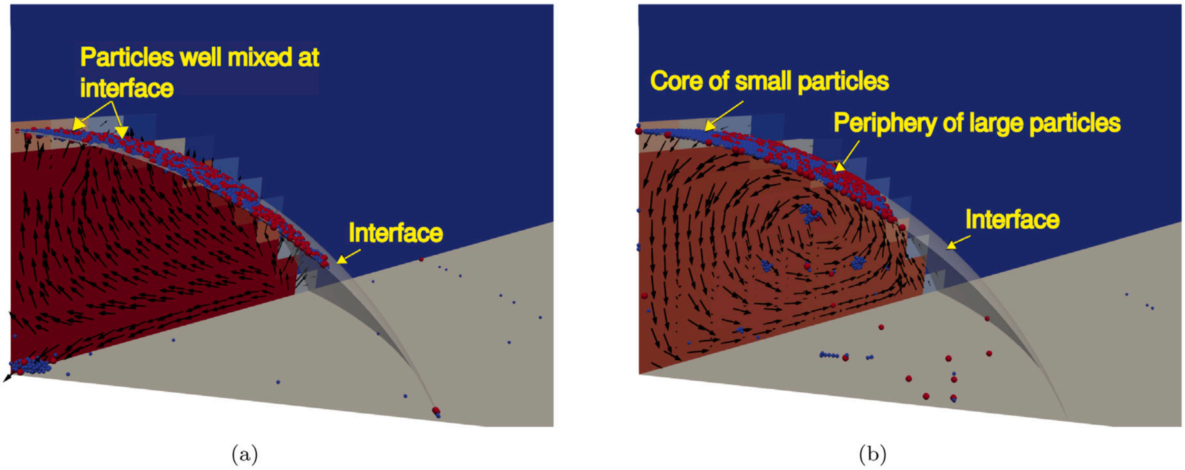

(a)

(b)

Fig. 14. Dispersion of particles in an evaporating ethanol droplet with contact angle $\theta_r = 60°$, where Marangoni stresses are **(a)** neglected and **(b)** considered.

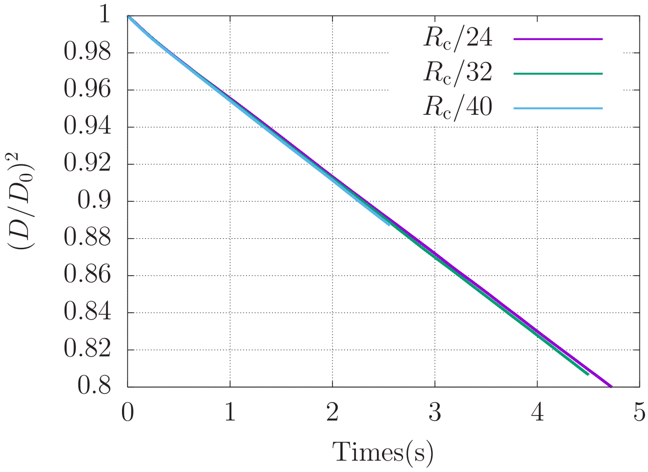

Fig. 15. Volume evolution for sessile droplet in case C4 with Marangoni flow and contact angle $\theta_c = 90°$ for three different resolutions.

line, where the evaporation rate is typically highest, the motion of the receding contact line drives fluid from the contact line to the apex. For the considered evaporating ethanol droplets, the flow induced by the receding motion of the contact line supersedes the capillary flow, leading to a resultant fluid flow from the contact line to the apex of the droplet in the absence of Marangoni stresses, as is observed in Fig. 14(a). In contrast, in the presence of Marangoni stresses, the Marangoni flow dominates over the other two flows, resulting in a classical single vortex flow, as seen in Fig. 14(b).

In Fig. 14(a), the dispersion of particles in case C1 is shown, where the contact angle $\theta_c = 60°$ and Marangoni flow is neglected. The fluid flow induced by the receding motion of the contact line moves the particles from the bulk of the droplet to the apex of the droplet, where the particles adsorb to the interface. Since the flow in this droplet is oriented predominantly in the direction normal to the interface, the adsorbed particles retain their position at the interface. Hence, there is no mechanism present that promotes a size-dependent sorting of the particles adsorbed at the interface. In one of the cases presented by Liu et al. (2019), the deposition of bidisperse polystyrene particles in a D_2O solution evaporating under constant contact angle conditions is investigated. The evaporation in their experiment proceeds isothermally and at a slower rate compared to ethanol droplet evaporation; as a result, the internal flow field and the resulting particle deposition arise from different mechanisms than those considered in the present study. It is shown that under fast evaporation conditions, capillary flow transports smaller particles towards the contact line due to their lower Stokes number, while larger particles tend to accumulate near the center of the droplet. In contrast, during slow evaporation as studied by Liu et al. (2019), the particles remain suspended in the liquid and are captured by the interface, leading to reduced segregation of the bidisperse particle population. In contrast, if Marangoni stresses are considered, the resulting flow along the interface promotes particle interactions, which in turn creates gaps between the particles that are preferentially filled by the small particles, see Fig. 14(b). As a result, the small particles agglomerate near the stagnation point of the flow at the apex of the droplet, with the large particles gathering around this agglomeration of small particles. We can, therefore, conclude that the dominant flow contribution associated with the thermocapillary Marangoni stresses is responsible for the size-based sorting of particles adsorbed at the gas-liquid interface.

7. Conclusions

In this study, we have investigated the behavior of bidisperse particles in evaporating sessile droplets with a moving contact line. To this end, we have used a finite-volume method to model the gas-liquid fluid flow, in conjunction with Lagrangian particle tracking to model the behavior of the particles. Our study has focused on the influence of thermocapillary Marangoni stresses and the contact angle of the droplet on the fluid flow and the particle dispersion inside an ethanol droplet evaporating on a heated substrate.

Several interesting conclusions can be drawn from the results of this study. In the absence of Marangoni flow, the flow induced by the receding contact line moves the fluid from the contact line to the apex of the droplet and dominates the flow to the contact line driven by evaporation, irrespective of the contact angle of the droplet. The presence of Marangoni flow promotes evaporation when the contact angle is less than 90°, due to thermal convective mixing and low thermal resistance. However, when the contact angle exceeds 90°, the impact of the Marangoni flow decreases, resulting in a slower evaporation rate. This happens because of the increased thermal resistance, which is caused by the tall shape of the droplet and the decrease in the liquid–solid contact area, leading to a diminished effective thermal conductivity.

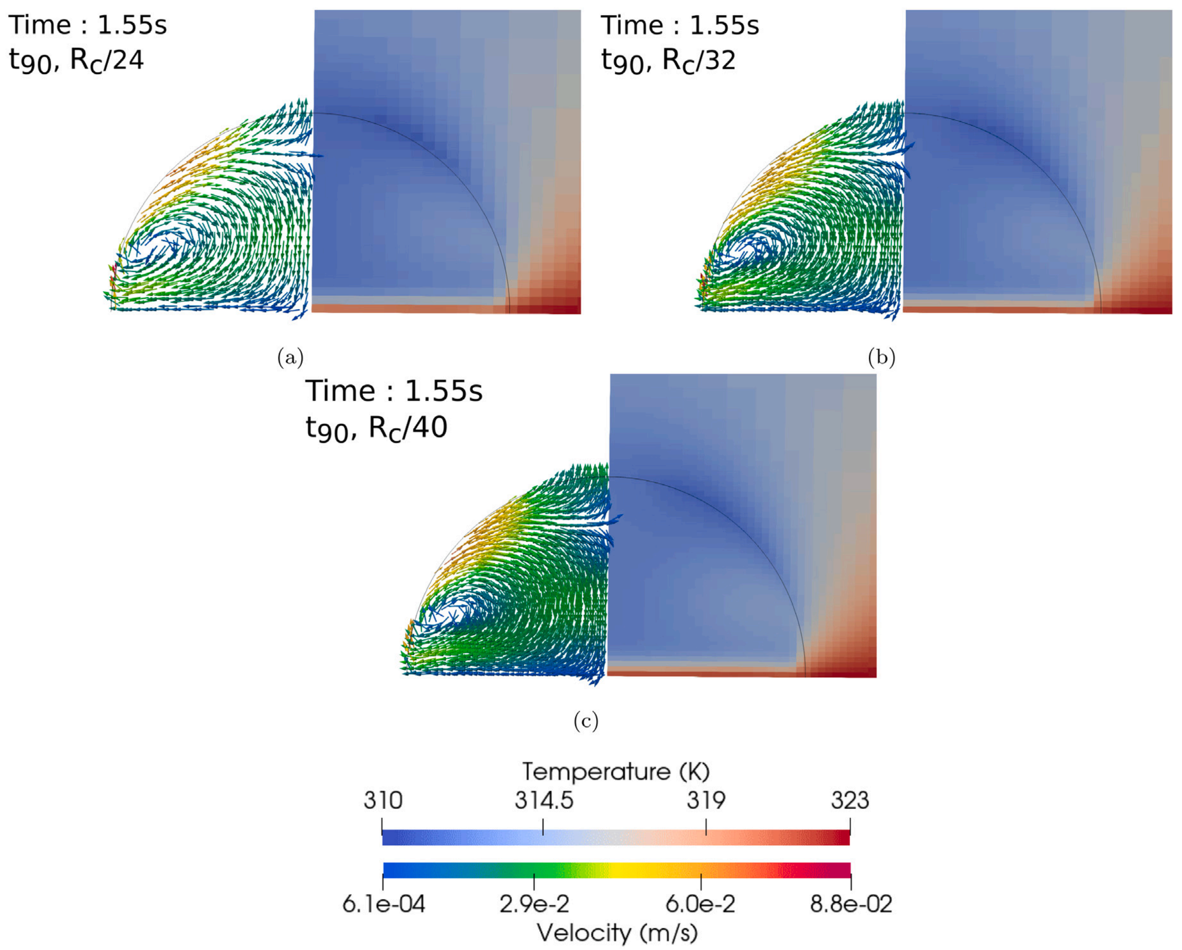

Fig. 16. Velocity and temperature plots for the cases including the Marangoni stresses, C4, where $\theta_c = 90°$, with different mesh resolutions. The left side of each figure shows the velocity vectors, of which the lengths are scaled with the color function and the color of the vectors shows their magnitude. The right side of each figure shows the temperature. **(a)** C4, $R_c/24$, t_{90},**(b)** C4, $R_c/32$, t_{90},**(c)** C4, $R_c/40$, t_{90}.

The Marangoni flow and the flow induced by the receding contact line both move the particles towards the apex of the droplet, although along different paths. With respect to the particles, the flow originating from Marangoni stresses has been identified as the mechanism driving the self-sorting of the bidisperse particles adsorbed at the interface. As a result of this self-sorting process, the small particles agglomerate at the apex of the droplet and the large particles surround this agglomeration of small particles.

These findings provide insights into controlling the dispersion and agglomeration of particles in evaporating sessile droplets by manipulating the surface wettability, heating conditions, and particle characteristics. This understanding has potential applications in fields such as inkjet printing, microfabrication, and coatings, where uniform or patterned particle deposition is desired. Although the model provides insightful results regarding the dispersion of particles in a sessile droplet, it should be noted that the model assumes one-way coupling of fluid and particles.

CRediT authorship contribution statement

Aman Kumar Jain: Writing – original draft, Validation, Software, Investigation, Formal analysis, Data curation. **Fabian Denner:** Writing – review & editing, Writing – original draft, Supervision, Software, Project administration, Methodology, Investigation, Funding acquisition, Formal analysis, Conceptualization. **Berend van Wachem:** Writing – review & editing, Writing – original draft, Supervision, Software, Resources, Project administration, Methodology, Funding acquisition, Formal analysis, Conceptualization.

Declaration of competing interest

The authors declare that they have no known competing financial interests or personal relationships that could have appeared to influence the work reported in this paper.

Acknowledgments

This research was funded by the Deutsche Forschungsgemeinschaft (DFG, German Research Foundation), grant number 452916560.

Appendix A. Mesh-independence study

A mesh-independence study for case C4 with Marangoni flow, substrate temperature $T_s = 50\,°\mathrm{C}$ and contact angle $\theta_c = 90°$ is carried out, by resolving the initial contact radius by 24, 32, and 40 cells. The results of the evolution of the droplet volume for the three different resolutions, shown in Fig. 15, exhibit excellent agreement, indicating

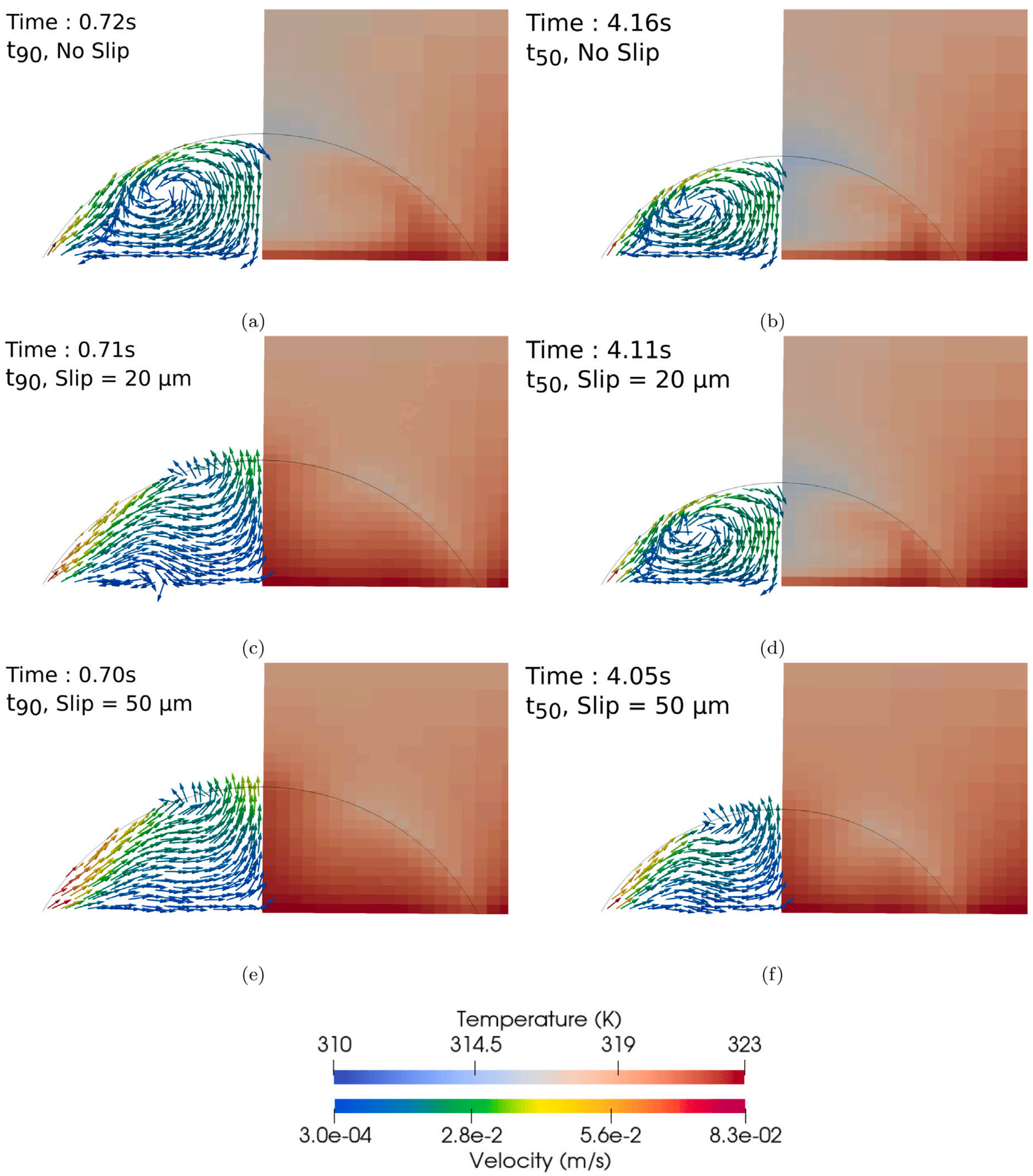

Fig. 17. Velocity and temperature plots for the cases including the Marangoni stresses, C2, where $\theta_c = 60°$, with different slip length. Velocity vector plots on left, where the color indicates the velocity magnitude. Contour plots of the temperature on the right. **(a)** C2, no-slip, t_{90},**(b)** C2, no-slip, t_{50},**(c)** C2, slip length = 20 μm, t_{90},**(d)** C2, slip length = 20 μm, t_{50},**(e)** C2, slip length = 50 μm, t_{90},**(d)** C2, slip length = 50 μm, t_{50}.

that the evaporation dynamics are mesh independent. In addition, Fig. 16 shows the velocity and temperature distribution inside the droplet. Both the velocity and temperature are in qualitatively very good agreement for the three mesh resolutions.

Appendix B. Slip length

To study the slip-length model used to simulate the moving contact line for an evaporating sessile droplet, three different cases are considered for case C2 with a contact angle 60° and accounting for Marangoni stresses: (i) a vanishing slip length (i.e. no slip), see Figs. 17(a) and 17(b), (ii) a slip length of 20 μm, see Figs. 17(c) and 17(d), and (iii) a slip length of 50 μm, see Figs. 17(e) and 17(f). In general, we can observe in Fig. 17 that an increasing slip length suppresses the formation of the vortex ring in the droplet and increases the temperature at the apex of the droplet. This stands in contrast to available experimental measurements (Zhu et al., 2021; Zhu and Shi, 2023) and other numerical studies (Paul and Dhar, 2023), which show that for a volatile sessile droplet evaporating with a freely moving contact line, the coldest region appears at the apex of the droplet. We, therefore, conclude that a no-slip boundary condition is the most appropriate choice for our study.

Data availability

The data that support the findings of this study are reproducible and data is openly available in the repository with DOI 10.5281/zenodo.15114147, available at https://doi.org/10.5281/zenodo.15114147.

References

Afkhami, S., Zaleski, S., Bussmann, M., 2009. A mesh-dependent model for applying dynamic contact angles to VOF simulations. J. Comput. Phys. 228, 5370–5389. http://dx.doi.org/10.1016/j.jcp.2009.04.027.

Allen, M.P., Tildesley, D.J., 1989. The Computer Simulation of Liquids, Vol. 42, Oxford University Press.

Barmi, M.R., Meinhart, C.D., 2014. Convective Flows in Evaporating Sessile Droplets. J. Phys. Chem. B 118, 2414–2421. http://dx.doi.org/10.1021/jp408241f.

Berteloot, G., Pham, C.T., Daerr, A., Lequeux, F., Limat, L., 2008. Evaporation-induced flow near a contact line: Consequences on coating and contact angle. EPL Eur. Letters 83, 14003. http://dx.doi.org/10.1209/0295-5075/83/14003.

Bhardwaj, R., 2018. Analysis of an Evaporating Sessile Droplet on a Non-Wetted Surface. Colloid Interface Sci. Commun. 24, 49–53. http://dx.doi.org/10.1016/j.colcom.2018.02.004.

Brackbill, J., Kothe, D., Zemach, C., 1992. Continuum Method for Modeling Surface Tension. J. Comput. Phys. 100, 335–354.

Chen, X., Chen, P.G., Ouazzani, J., LIu, Q., 2017. Numerical simulations of sessile droplet evaporating on heated substrate. Eur. Phys. J. Spec. Top. 226, 1325–1335. http://dx.doi.org/10.1140/epjst/e2016-60203-y.

Chen, R., Zhang, L., Zang, D., Shen, W., 2016. Blood drop patterns: Formation and applications. Adv. Colloid Interface Sci. 231, 1–14. http://dx.doi.org/10.1016/j.cis.2016.01.008.

Chhasatia, V.H., Sun, Y., 2011. Interaction of bi-dispersed particles with contact line in an evaporating colloidal drop. Soft Matter 7 (10135), http://dx.doi.org/10.1039/c1sm06393f.

Cundall, P., Strack, O.D.L., 1979. A discrete numerical model for granular assemblies. Géotechnique 29, 47–65. http://dx.doi.org/10.1680/geot.1979.29.1.47.

Das, S., Dey, A., Reddy, G., Sarma, D.D., 2017. Suppression of the Coffee-Ring Effect and Evaporation-Driven Disorder to Order Transition in Colloidal Droplets. J. Phys. Chem. Lett. 8, 4704–4709. http://dx.doi.org/10.1021/acs.jpclett.7b01814.

Dash, S., Garimella, S.V., 2013. Droplet Evaporation Dynamics on a Superhydrophobic Surface with Negligible Hysteresis. Langmuir 29, 10785–10795. http://dx.doi.org/10.1021/la402784c.

Deegan, R.D., 2000. Pattern formation in drying drops. Phys. Rev. E 61, 475–485. http://dx.doi.org/10.1103/PhysRevE.61.475.

Deising, D., Marschall, H., Bothe, D., 2016. A unified single-field model framework for Volume-Of-Fluid simulations of interfacial species transfer applied to bubbly flows. Chem. Eng. Sci. 139, 173–195. http://dx.doi.org/10.1016/j.ces.2015.06.021.

Denner, F., Evrard, F., van Wachem, B., 2020. Conservative finite-volume framework and pressure-based algorithm for flows of incompressible, ideal-gas and real-gas fluids at all speeds. J. Comput. Phys. 409, 109348. http://dx.doi.org/10.1016/j.jcp.2020.109348.

Denner, F., van Wachem, B., 2014a. Compressive VOF method with skewness correction to capture sharp interfaces on arbitrary meshes. J. Comput. Phys. 279, 127–144. http://dx.doi.org/10.1016/j.jcp.2014.09.002.

Denner, F., van Wachem, B., 2014b. Fully-coupled balanced-force VOF framework for arbitrary meshes with least-squares curvature evaluation from volume fractions. Numer. Heat Transf. Part B: Fundam. 65, 218–255. http://dx.doi.org/10.1080/10407790.2013.849996.

Derjaguin, B., Muller, V., Toporov, Y., 1975. Effect of contact deformations on the adhesion of particles. J. Colloid Interface Sci. 53, 314–326. http://dx.doi.org/10.1016/0021-9797(75)90018-1.

Diddens, C., Tan, H., Lv, P., Versluis, M., Kuerten, J.G.M., Zhang, X., Lohse, D., 2017. Evaporating pure, binary and ternary droplets: Thermal effects and axial symmetry breaking. J. Fluid Mech. 823, 470–497. http://dx.doi.org/10.1017/jfm.2017.312.

Erbil, H.Y., 2012. Evaporation of pure liquid sessile and spherical suspended drops: A review. Adv. Colloid Interface Sci. 170, 67–86. http://dx.doi.org/10.1016/j.cis.2011.12.006.

Erdem, A.K., Denner, F., Biancofiore, L., 2024. Numerical Analysis of the Dispersion and Deposition of Particles in Evaporating Sessile Droplets. Langmuir 40, 13428–13445. http://dx.doi.org/10.1021/acs.langmuir.4c00680.

Gelderblom, H., Diddens, C., Marin, A., 2022. Evaporation-driven liquid flow in sessile droplets. Soft Matter 18, 8535–8553. http://dx.doi.org/10.1039/D2SM00931E.

Gupta, S., Thombare, M.R., Patil, N.D., 2023. Pinning and Depinning Dynamics of an evaporating sessile droplet containing mono- and Bidispersed Colloidal Particles on a Nonheated/heated hydrophobic substrate. Langmuir http://dx.doi.org/10.1021/acs.langmuir.2c03270.

Gurrala, P., Katre, P., Balusamy, S., Banerjee, S., Sahu, K.C., 2019. Evaporation of ethanol-water sessile droplet of different compositions at an elevated substrate temperature. Int. J. Heat Mass Transfer 145, 118770. http://dx.doi.org/10.1016/j.ijheatmasstransfer.2019.118770.

Haroun, Y., Legendre, D., Raynal, L., 2010. Volume of fluid method for interfacial reactive mass transfer: Application to stable liquid film. Chem. Eng. Sci. 65, 2896–2909.

Hu, H., Larson, R.G., 2002. Evaporation of a Sessile Droplet on a Substrate. J. Phys. Chem. B 106, 1334–1344. http://dx.doi.org/10.1021/jp0118322.

Hu, H., Larson, R.G., 2005. Analysis of the Microfluid Flow in an Evaporating Sessile Droplet. Langmuir 21, 3963–3971. http://dx.doi.org/10.1021/la047528s.

Huh, C., Scriven, L., 1971. Hydrodynamic model of steady movement of a solid/liquid/fluid contact line. J. Colloid Interface Sci. 35, 85–101. http://dx.doi.org/10.1016/0021-9797(71)90188-3.

Iqbal, R., Matsumoto, A., Carlson, D., Peters, K.T., Funari, R., Sen, A.K., Shen, A.Q., 2022. Evaporation driven smart patterning of microparticles on a rigid-soft composite substrate. J. Colloid Interface Sci. 623, 927–937. http://dx.doi.org/10.1016/j.jcis.2022.05.087.

Jain, A.K., Denner, F., van Wachem, B., 2024. Dispersion of particles in a sessile droplet evaporating on a heated substrate. Int. J. Multiph. Flow 180, 104956. http://dx.doi.org/10.1016/j.ijmultiphaseflow.2024.104956.

Kazemi, M.A., Saber, S., Elliott, J.A., Nobes, D.S., 2021. Marangoni convection in an evaporating water droplet. Int. J. Heat Mass Transfer 181, 122042. http://dx.doi.org/10.1016/j.ijheatmasstransfer.2021.122042.

Kothe, D.D.B., Rider, W.J., Mosso, S.S., Brock, J.J., 1996. Volume tracking of interfaces having surface tension in two and three dimensions. AIAA 96–0859, 25.

Larson, R.G., 2014. Transport and deposition patterns in drying sessile droplets. AIChE J. 60, 1538–1571. http://dx.doi.org/10.1002/aic.14338.

Lebedev-Stepanov, P., Vlasov, K., 2013. Simulation of self-assembly in an evaporating droplet of colloidal solution by dissipative particle dynamics. Colloids Surfaces A: Physicochem. Eng. Asp. 432, 132–138. http://dx.doi.org/10.1016/j.colsurfa.2013.05.012.

Li, S., Marshall, J.S., Liu, G., Yao, Q., 2011. Adhesive particulate flow: The discrete-element method and its application in energy and environmental engineering. Prog. Energy Combust. Sci. 37, 633–668. http://dx.doi.org/10.1016/j.pecs.2011.02.001.

Liu, W., Midya, J., Kappl, M., Butt, H.J., Nikoubashman, A., 2019. Segregation in Drying Binary Colloidal Droplets. ACS Nano 13, 4972–4979. http://dx.doi.org/10.1021/acsnano.9b00459.

Maes, J., Soulaine, C., 2020. A unified single-field Volume-of-Fluid-based formulation for multi-component interfacial transfer with local volume changes. J. Comput. Phys. 402, 109024. http://dx.doi.org/10.1016/j.jcp.2019.109024.

Marschall, H., Hinterberger, K., Schüler, C., Habla, F., Hinrichsen, O., 2012. Numerical simulation of species transfer across fluid interfaces in free-surface flows using OpenFOAM. Chem. Eng. Sci. 78, 111–127. http://dx.doi.org/10.1016/j.ces.2012.02.034.

Mindlin, R.D., Deresiewicz, H., 1953. Elastic spheres in contact under varying oblique forces. J. Appl. Mech 20, 327–344.

Mondal, R., Lama, H., Sahu, K.C., 2023. Physics of drying complex fluid drop: Flow field, pattern formation, and desiccation cracks. Phys. Fluids 35, 061301. http://dx.doi.org/10.1063/5.0153682.

Nguyen, T.A.H., Hampton, M.A., Nguyen, A.V., 2013. Evaporation of Nanoparticle Droplets on Smooth Hydrophobic Surfaces: The Inner Coffee Ring Deposits. J. Phys. Chem. C 117, 4707–4716. http://dx.doi.org/10.1021/jp3126939.

Paul, A., Dhar, P., 2023. Transients of Marangoni and Stefan advection dynamics during generic sessile droplet evaporation. Phys. Fluids 35, 102022. http://dx.doi.org/10.1063/5.0171215.

Petsi, A.J., Burganos, V.N., 2008. Stokes flow inside an evaporating liquid line for any contact angle. Phys. Rev. E 78, 036324. http://dx.doi.org/10.1103/PhysRevE.78.036324.

Shang, X., Chen, H., Nguyen, T.B., Tran, T., 2024. Numerical investigation of evaporation-induced flow around sessile droplets using a sharp-interface algebraic VOF approach. Int. J. Heat Mass Transfer 231, 125849. http://dx.doi.org/10.1016/j.ijheatmasstransfer.2024.125849.

Snoeijer, J.H., Andreotti, B., 2013. Moving Contact Lines: Scales, Regimes, and Dynamical Transitions. Annu. Rev. Fluid Mech. 45, 269–292. http://dx.doi.org/10.1146/annurev-fluid-011212-140734.

Tomas, J., 2007. Adhesion of ultrafine particles—A micromechanical approach. Chem. Eng. Sci. 62, 1997–2010. http://dx.doi.org/10.1016/j.ces.2006.12.055.

Tsuji, Y., Tanaka, T., Ishida, T., 1992. Lagrangian numerical simulation of plug flow of cohesionless particles in a horizontal pipe. Powder Technol. 71, 239–250.

Vassileva, N.D., van den Ende, F., Mellema, J., 2005. Capillary Forces between Spherical Particles Floating at a Liquid-Liquid Interface. Langmuir 21, 11190–11200. http://dx.doi.org/10.1021/la051186o.

Vella, D., Mahadevan, L., 2005. The Cheerios effect. Am. J. Phys. 73, 817–825. http://dx.doi.org/10.1119/1.1898523.

van Wachem, K., Remmelgas, J., Niklasson-Björn, I., 2017. Simulation of Dry Powder Inhalers: Combining Micro-Scale, Meso-Scale and Macro-Scale Modeling. AIChE J. 63, 501–516. http://dx.doi.org/10.1002/aic.15424.

Wang, F.C., Wu, H.A., 2013. Pinning and depinning mechanism of the contact line during evaporation of nano-droplets sessile on textured surfaces. Soft Matter 9 (5703), http://dx.doi.org/10.1039/c3sm50530h.

Wen, C., Yu, Y., 1966. Mechanics of fluidization. Chem. Eng. Prog. Symp. Ser 62, 100–111.

Wilson, R., Dini, D., van Wachem, B., 2016. A numerical study exploring the effect of Particle Properties on the Fluidization of Adhesive Particles. AIChE J. 62, 1467–1477. http://dx.doi.org/10.1002/aic.15162.

Yang, K.C., Wang, C., Hu, T.Y., Lin, H.P., Cho, K.H., Chen, L.J., 2020. Self-pinning of silica suspension droplets on hydrophobic surfaces. J. Colloid Interface Sci. 579, 212–220. http://dx.doi.org/10.1016/j.jcis.2020.06.059.

Yoo, H., Kim, C., 2015. Experimental studies on formation, spreading and drying of inkjet drop of colloidal suspensions. Colloids Surfaces A: Physicochem. Eng. Asp. 468, 234–245. http://dx.doi.org/10.1016/j.colsurfa.2014.12.032.

Zang, D., Tarafdar, S., Tarasevich, Y.Y., Choudhury, M.Dutta., Dutta, T., 2019. Evaporation of a Droplet: From physics to applications. Phys. Rep. 804, 1–56. http://dx.doi.org/10.1016/j.physrep.2019.01.008.

Zanutto, C.P., Paladino, E.E., Evrard, F., van Wachem, B., Denner, F., 2022. Modeling of interfacial mass transfer based on a single-field formulation and an algebraic VOF method considering non-isothermal systems and large volume changes. Chem. Eng. Sci. 247, 116855. http://dx.doi.org/10.1016/j.ces.2021.116855.

Zhu, J.L., Feng, L., Shi, W.Y., 2021. Influence of thermal properties on hydrothermal waves in evaporating sessile droplets. Phys. Fluids 33, 102107. http://dx.doi.org/10.1063/5.0064888.

Zhu, J.L., Shi, W.Y., 2019. Longitudinal roll patterns of Marangoni instability in an easily volatile sessile droplet evaporating at constant contact angle mode. Int. J. Heat Mass Transfer 134, 1283–1291. http://dx.doi.org/10.1016/j.ijheatmasstransfer.2019.02.068.

Zhu, J.L., Shi, W.Y., 2021. Hydrothermal waves in sessile droplets evaporating at a constant contact angle mode. Int. J. Heat Mass Transfer 172, 121131. http://dx.doi.org/10.1016/j.ijheatmasstransfer.2021.121131.

Zhu, J.L., Shi, W.Y., 2023. Instability patterns of Marangoni flow in evaporating droplets on lyophobic surface. Int. Commun. Heat Mass Transfer 141, 106598. http://dx.doi.org/10.1016/j.icheatmasstransfer.2022.106598.

Zolotarev, P.A., Kolegov, K.S., 2022. Monte Carlo simulation of particle size separation in evaporating bi-dispersed colloidal droplets on hydrophilic substrates. Phys. Fluids 34, 017107. http://dx.doi.org/10.1063/5.0072083.